International Journal of Hydrogen Energy 236 (2026) 155250

Contents lists available at ScienceDirect

International Journal of Hydrogen Energy

journal homepage: www.elsevier.com/locate/he

Hydrogen low-pressure direct injection: 3D-CFD hollow cone injector model, flow and mixing analysis

B. Fil, C.J. Ramsay, K.K.J. Ranga Dinesh *

Energy Technology Research Group, School of Engineering, Faculty of Engineering and Physical Sciences, University of Southampton, Southampton, SO17 1BJ, UK

ARTICLE INFO

Keywords:
Hydrogen internal combustion engines
Low-pressure hydrogen direct injection
Hollow cone injector
Flow field and mixing
3D-CFD injector model

ABSTRACT

A three-dimensional unsteady Reynolds-averaged Navier-Stokes (URANS) modelling framework was employed to study the flow and mixing characteristics of a hydrogen low-pressure direct-injection process using a hollow-cone injector. The hollow-cone injector model was validated with experimental data, and a sensitivity analysis of numerical mesh, turbulence model, turbulent Schmidt number, and Courant-Friedrichs-Lewy number was carried out. Then, the local flow, mixing, and turbulence characteristics were investigated first by varying the injection pressure at a constant chamber pressure, then by varying the injector needle lift at a constant fuel mass. The results showed that increasing the fuel injection pressure at a constant needle lift resulted in increases in total injected fuel mass, axial penetration, radial penetration, and turbulent kinetic energy. Furthermore, elevating the needle lift while maintaining a constant fuel injection pressure also resulted in increases in total injected fuel mass, axial and radial penetrations, and turbulent kinetic energy. Analysis of the balance between needle lift and injection pressure, with fixed total injected fuel mass, shows that the case with 85 μm needle lift and 20.7 bar injection pressure exhibits increased axial penetration, while the case with 135 μm needle lift and 12.68 bar injection pressure e demonstrates increased radial penetration. The scenario involving a 35 μm needle lift and 51 bar injection pressure exhibits, on average, 35% and 20% higher turbulent kinetic energy compared to the 85 μm and 135 μm scenarios, respectively, and reaches the highest turbulent kinetic energy levels of 13 m^2/s^2, while the other two scenarios remained at 7.5 m^2/s^2; this represents an increase of approximately 75%. Additionally, in this case, distinct areas of elevated vorticity with strong shear layers and substantial jet momentum were observed while exhibiting minimal jet disturbance.

1. Introduction

The transport sector accounts for more than 15% of global carbon dioxide emissions [1,2]. Hydrogen internal combustion engine (H_2ICE) technology is emerging as a potential solution for future propulsion applications to decarbonise the heavy-duty transport sector [3–6]. In H_2ICE concepts, the fuel injection process can play a key role in determining the engine power output [7], efficiency [8] and emissions [9]. The fuel injection process of H_2ICE is categorised into two types: hydrogen port injection (H_2PI) and hydrogen direct injection (H_2DI). H_2PI engines exhibit a reduced power output [10] and are more prone to backfiring and engine knocking [11,12]. Conversely, H_2DI mitigates the pre-ignition challenges by decreasing the duration of interaction between the hydrogen and air mixtures [13] and prevents the risk of backfire and reduction in volumetric efficiency, because injected hydrogen does not replace intake air [14]. In H_2DI engines, a critical characteristic is the fuel–air mixing and jet formation, since it significantly affects combustion efficiency, engine performance, and emissions [15]. An essential design characteristic for H_2 injectors is the orientation of the needle opening, namely, whether it is inward or outward fuel induction into the engine [16]. In order to achieve accurate and efficient fuel delivery, aiming for high efficiency and low-emission H_2ICEs, advanced H_2DI fuel injector designs are required.

Recent research has focused on the application of outwardly opening hollow-cone H_2 low-pressure direct injectors, noted for their unique annular orifice design. H_2DI hollow-cone injector facilitates substantial enhancement in the volume of injected hydrogen relative to circular orifice injectors [17] and operates under low-pressure injection conditions. Its ability to feed fuel to the engine via a cost-effective pumping system using controlled pressure from H_2 gaseous storage tanks at 35 MPa or 70 MPa is its main advantage over high-pressure direct injection. Furthermore, H_2 low-pressure direct injection reduces lubrication and sealing requirements, thereby minimising leakage potential. This

* Corresponding author.
E-mail address: dinesh.kahanda-koralage@soton.ac.uk (K.K.J. Ranga Dinesh).

https://doi.org/10.1016/j.ijhydene.2026.155250
Received 7 February 2026; Received in revised form 18 April 2026; Accepted 23 April 2026
Available online 28 April 2026

Abbreviations

AMR	Adaptive mesh refinement
aSOI	After start of the injection
CFL	Courant-Friedrichs-Lewy
ECN	Engine combustion network
HDEV	Hochdruck-Einspritzventil
H_2DI	Hydrogen direct injection
H_2ICE	Hydrogen internal combustion engine
H_2PI	Hydrogen port injection
LES	Large eddy simulations
MAPE	Mean absolute percentage error
NPR	Nozzle pressure ratio
PISO	Pressure implicit with splitting of operators
RNG	Renormalization group
Sct	Turbulent Schmidt number
SST	Shear stress transport
3D-CFD	Three-dimensional computational fluid dynamics.

technology enables early injection to provide adequate H_2 fuel mass into the engine, resulting in a more uniform lean homogeneous fuel-air mixture, potentially enhancing thermal efficiency and decreasing NO_x emissions [18–22]. Due to all these benefits, low-pressure H_2DI is gaining attention among H_2 fuel injector manufacturers for H_2ICE development.

Previous experimental [14,23–33] and computational fluid dynamics (CFD) based numerical investigations [34–38] indicate that the H_2DI strategy using a hollow-cone injector, encompassing nozzle design, needle lift, injection pressure, ambient pressure, and pressure ratio, significantly influences jet formation, penetration length, turbulent kinetic energy, vorticity, and the subsequent mixing and combustion characteristics. For example, Wu et al. [14] proved that the injected mass exhibits a linear correlation with both injection pressure and duration. Hu et al. [23] found that the projection area, axial and radial penetrations increase with elevated injection pressure. Montanaro et al. [24] observed that at low back pressure, increasing injection pressure primarily enhances radial dispersion, with minimal effect on axial penetration. Pucillo et al. [25] discovered that interaction with the chamber walls primarily determines the jet shape, and the positive recess yields a hollow-cone jet shape, while the negative recess results in a jet shape characteristic of the solid-cone configuration. Huang et al. [26] reported that jet penetration initially increases most rapidly during the early stage, transitions to a slower growth rate in the intermediate stage, and exhibits a decelerated increase in the late stage. Wang et al. [27] proposed a non-dimensional scaling correlation for axial penetration of H_2 jets, applicable within a pressure ratio range of 10 to 140. Lee et al. [28] detected that the gas phase of hydrogen can stagnate near the injector, resulting in a rich mixture that may lead to decreased combustion efficiency, which can be eliminated either by increasing the nozzle angle or decreasing the ambient pressure. Kuensch et al. [29] identified that during the initial phase, the jet exhibits two distinct independent layers in its cross-sectional area. Subsequently, the gas jet converges onto the central axis, leading to the formation of a singular jet that predominantly propagates along the axial direction. Ge et al. [30] studied combustion and knocking characteristics of a direct injection H_2 engine with low injection pressure. They found that advancing spark ignition timing up to a certain limit accelerates the combustion process and heat release rate in a low-pressure H_2 direct injection engine. The study carried out by Wang et al. [31] designed a dedicated low-pressure direct injection H_2 spark ignition engine and examined the impact of excess air ratio and spark timing on engine performance. Lu et al. [32] have investigated the impact of different mixing strategies and subsequent combustion modes, such as homogenous and stratified combustion, in a direct injection H_2 spark ignition engine with higher injection pressure above 100 bar. Their study demonstrated that appropriate injection timing based on operating conditions is crucial to achieve balance between performance and emissions in a H_2 direct injection engine. The study reported by Bayer et al. [33] investigated high-pressure direct injection process with injection pressure close to 200 bar for H_2 combustion engine. They have analysed a high-pressure H_2 injected jet-guided spark ignition non-premixed combustion mode in an H_2ICE engine in order to mitigate abnormal combustion while maintaining a reasonable power density and low emissions.

Coratella et al. [34] observed shock waves to form at the needle tip under conditions of a high-pressure ratio. Additionally, increased pressure ratios enhance the pressure gradient perpendicular to the gas flow along the needle surface, thereby intensifying the Coanda effect. Fleischmann et al. [35] observed the Coanda effect with short recess positions, and no advantages of large eddy simulations (LES) over URANS were identified, attributed to the fine discretisation employed. Tang et al. [36] discovered that the probability density function of axial and radial hydrogen mole concentration aligns with the Gaussian distribution. Lee et al. [37] identified the development of vortical flow in the interior region of the jet, where the pressure was much lower than on the jet's outer side. Also, multiple injections were found to be superior to a single injection in creating a desirable hydrogen-air combination close to the spark plug. Huang et al. [38] have investigated low-pressure H_2 direct injection in engine configuration. They proposed different mixing strategies with respect to injection pressure and injection timing in order to achieve in-cylinder homogeneous versus stratified mixing for different engine operating conditions. The study of Shimmura et al. [19] analysed how high thermal efficiency can be obtained with a low-pressure H_2 direct injection by optimising the H_2 jet-guided fuel injection process.

Further studies were also reported for comparison of flow and mixing characteristics between different H_2 injector geometries. For example, Cabezas et al. [39] found that single-hole and multi-hole injector nozzles exhibit higher penetration lengths and enhanced mixing efficiency compared to a hollow-cone injector nozzle. Moreno-Cabezas et al. [40] indicated that multi-hole injectors enhance fuel-air mixing by increasing turbulent interactions, which resulted in a more homogeneous fuel-air mixture and a reduction in stratification. Houidi et al. [41] found that the hollow-cone injector exhibits a broader probability density function distribution that exceeds stoichiometric limits, and the multi-hole nozzle generates a more confined distribution, maintaining the equivalence ratio at levels below 0.5. The investigation conducted by Yeganeh et al. [42] revealed that the single-hole jet exhibits the smallest cross-sectional area and the highest penetration speed, while the double-hole jet demonstrates the largest cross-sectional area and the lowest penetration speed.

Although the above-noted 3D-CFD modelling studies have explored low-pressure H_2DI strategy and H_2 jet mixing in a constant-volume chamber, there are research gaps in the literature, for example, sensitivity and error analyses of the key CFD model parameters within the context of URANS simulation approach to accurately predict jet mixing characteristics and the trade-off between hollow cone injector needle lift and injection pressure. Both injector needle lift and injection pressure play an important role for low-pressure H_2DI in a H_2 combustion engine, but their individual impact on jet mixing have not been fully investigated. The present study focuses on filling this research gap by proposing a comprehensive 3D-CFD injector model and simultaneously evaluating the key 3D-CFD model parameters, such as dynamic meshing techniques, turbulence model, turbulent Schmidt number and CFL number, within the context of the URANS simulation approach. The study also examines the influence of fuel injection pressure while maintaining a constant chamber pressure, as well as the effect of needle lift while maintaining a constant total injected fuel mass on local flow dynamics, mixing characteristics, and turbulence generation. This will evaluate the trade-off between needle lift and fuel injection pressure to

Table 1
Summary of numerical methods and models employed during simulations.

Description	Parameter	Method/Model/Mechanism
Numerical discretisation	Scheme	Finite-volume
Solver	Type	Density-based
	Scheme	PISO
Turbulence modelling	Turbulence	RNG k-ε
Pressure-velocity coupling	Scheme	Generalized Rhie-Chow scheme
	Gradient	Second-order central scheme
	Density	Second-order central scheme
	Momentum	Second-order central scheme
Spatial discretisation	Energy	Second-order central scheme
	k	First-order upwind scheme
	ε	First-order upwind scheme
Temporal discretisation	Time	Transient Solver (first-order implicit Euler)

achieve optimal mixing performance, which can provide tangible design guidelines for low-pressure H_2DI with a hollow cone injector. Although different fuel injector geometries, such as hollow-cone, single-hole and multi-hole, are emerging as options for both low- and high-pressure H_2DI strategies, in this investigation we have selected the hollow-cone injector geometry mainly due to the availability of the experimental data for 3D-CFD numerical model validation for low-pressure H_2 fuel injection in a constant volume chamber. The paper is organised as follows. Sections 2 and 3 present numerical methodology and results and discussion, respectively. Section 4 provides the main conclusions of this study.

2. 3D-CFD hollow cone injector model set up and numerical methodology

A 3D-CFD URANS hollow cone injector model was set up to simulate compressible turbulent non-reacting H_2 jet mixing characteristics in a constant-volume chamber, utilising CONVERGE 4.1.2 software. All simulations were performed on the University of Southampton IRIDIS 6 high-performance computing cluster.

2.1. Mathematical equations

The compressible governing equations for mass (Eq. (1)), momentum (Eq. (2)), energy (Eq. (3)), and species transport (Eq. (4)) solved in the simulations are given by:

$$\frac{\partial \rho}{\partial t}+\frac{\partial \rho u_i}{\partial x_i}=0 \tag{1}$$

$$\frac{\partial \rho u_i}{\partial t}+\frac{\partial \rho u_i u_j}{\partial x_j}=-\frac{\partial P}{\partial x_i}+\frac{\partial}{\partial x_j}\left(\mu\left(\frac{\partial u_i}{\partial x_j}+\frac{\partial u_j}{\partial x_i}\right)+\left(\mu'-\frac{2}{3}\mu\right)\left(\frac{\partial u_k}{\partial x_k}\delta_{ij}\right)\right) \tag{2}$$

$$\frac{\partial \rho e}{\partial t}+\frac{\partial \rho e u_j}{\partial x_j}=-P\frac{\partial u_j}{\partial x_j}+\frac{\partial}{\partial x_j}\left(K\frac{\partial T}{\partial x_j}\right)+\sigma_{ij}\frac{\partial u_i}{\partial x_j}+\frac{\partial}{\partial x_j}\left(\rho\sum_m D_{tot}h_m\frac{\partial Y_m}{\partial x_j}\right) \tag{3}$$

$$\frac{\partial \rho_m}{\partial t}+\frac{\partial \rho_m u_j}{\partial x_j}=\frac{\partial}{\partial x_j}\left(\rho D_{tot}\frac{\partial Y_m}{\partial x_j}\right) \tag{4}$$

where u is velocity, ρ is density, P is pressure, μ is viscosity, μ′ is the dilatational viscosity (set to zero), δ_{ij} is the Kronecker delta, Y_m is the mass fraction of species m, D_{tot} is the species total diffusivity, e is the specific internal energy, K is the thermal conductivity, and h_m is the species-specific enthalpy. The species total diffusivity was calculated as a summation of molecular and turbulent diffusivities, and mixture-averaged diffusivity, viscosity, and thermal conductivity coefficients were applied when solving the species and energy transport equations [43–47]. For compressible flows, an equation of state is required to couple density, pressure, and temperature. The Redlich-Kwong equation of state was used to capture the real gas effects. Additional equations were solved for turbulence modelling using the renormalization group (RNG) k-ε method.

2.2. Numerical methods

All numerical simulations were conducted utilising a density-based solver to resolve the conservation equations via the finite volume method. A modified version of the density-based pressure implicit with splitting of operators (PISO) scheme was utilised, and the Rhie-Chow scheme was employed as the pressure-velocity coupling method. The mass, momentum, energy, and species equations were spatially discretised using a second-order central scheme, while the turbulence model equations were solved using a first-order upwind method. The first-order implicit Euler method was chosen for time advancement. The Redlich-Kwong equation of state was utilised to model thermodynamic properties. Table 1 depicts and summarises the numerical methods employed in the study.

2.3. Hollow cone injector specifications and dynamic meshing approach

The H_2 fuel injection process modelled in this study utilised a cylindrical constant volume chamber with a 100 mm diameter and 50 mm length as the computational domain. The injector utilised in the present study is the Bosch (HDEV4) hollow-cone injector with an outward-opening needle [48]. A majority of the experimental data is easily accessible for the numerical model validation of low-pressure H_2 injection using the hollow cone injector. That is why we employed this configuration for 3D-CFD model validation. The left side of Fig. 1a displays a cross-section obtained from the X-ray scan images [49], whereas the right side illustrates the reproduced interior geometry, incorporating the needle lift. In order to address the complexities inherent in modelling the internal flow dynamics of the nozzle and to facilitate detailed simulations of fuel injection, a simplified variant of the Bosch HDEV4 injector has been considered, as depicted in Fig. 1b, retaining the original external profile, spray angle, and needle lift characteristics. This study's only limitation is the consideration of a simplified injector version that maintains its original external profile, spray angle, and needle lift characteristics. This is intended to eliminate the complexities associated with modelling the internal flow dynamics of the nozzle. The modifications were implemented to enhance computational efficiency and ensure simulation stability, while maintaining the essential characteristics of the flow field behaviour. While it is acknowledged that small-scale flow details may experience some degree of influence, it is anticipated that the primary performance trends is accurately represented.

A base grid size of 1 mm was applied to the domain. Level 4 and 2 fixed embeddings were implemented on the interfaces between the injector and chamber and the upper surface of the chamber, respectively. To enhance the representation of flow dynamics within the nozzle and its surrounding region, a Level 6 fixed embedding was implemented in a conical configuration, originating from the inlet surface and extending along the direction of injection. Additionally, a permanent level 3 adaptive mesh refinement (AMR) strategy was employed in the chamber such that the mesh was refined for H_2 mass fractions between 0.01 and 1 to properly capture jet propagation and spreading. The dynamic meshing strategies applied to the hollow cone injector model are illustrated in Fig. 1c.

2.4. H_2 hollow cone direct fuel injector model validation and sensitivity analysis of CFD parameters

In this section, CFD modelling results are compared with experimental data provided by Cabezas et al. [39] for the low-pressure H_2DI hollow cone injector model validation. Their experiments included the injection of H_2 using the Bosch HDEV4 injector (originally developed for

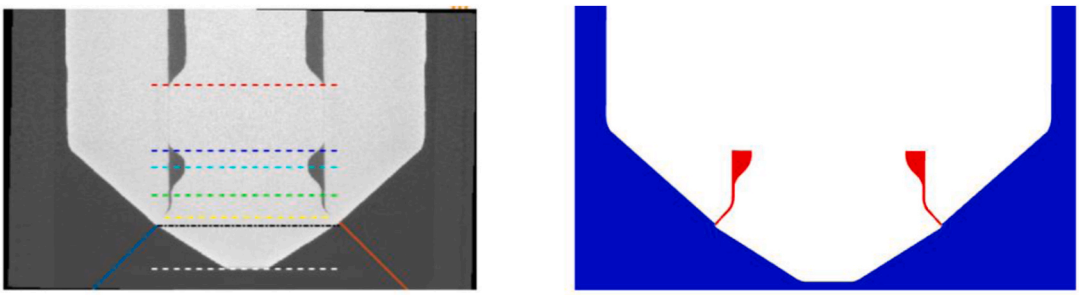

a)Bosch HDEV hollow-cone injector X-ray scan and reproduced internal geometry

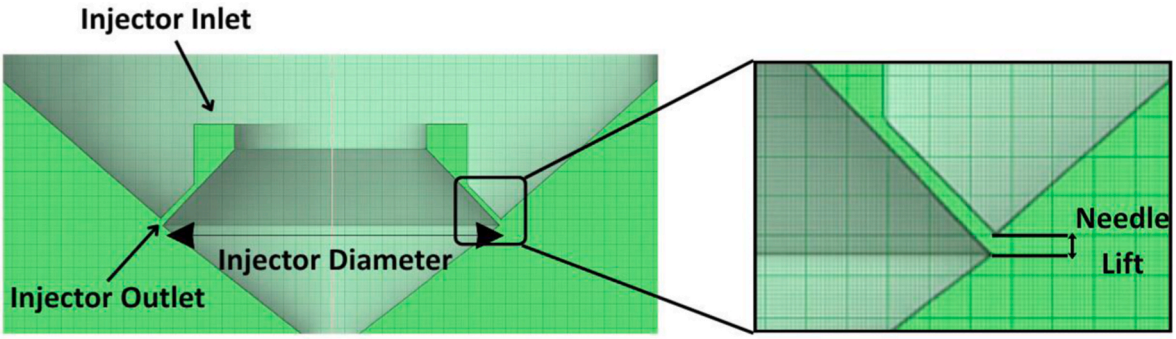

b)Bosch HDEV hollow-cone injector geometry after simplification

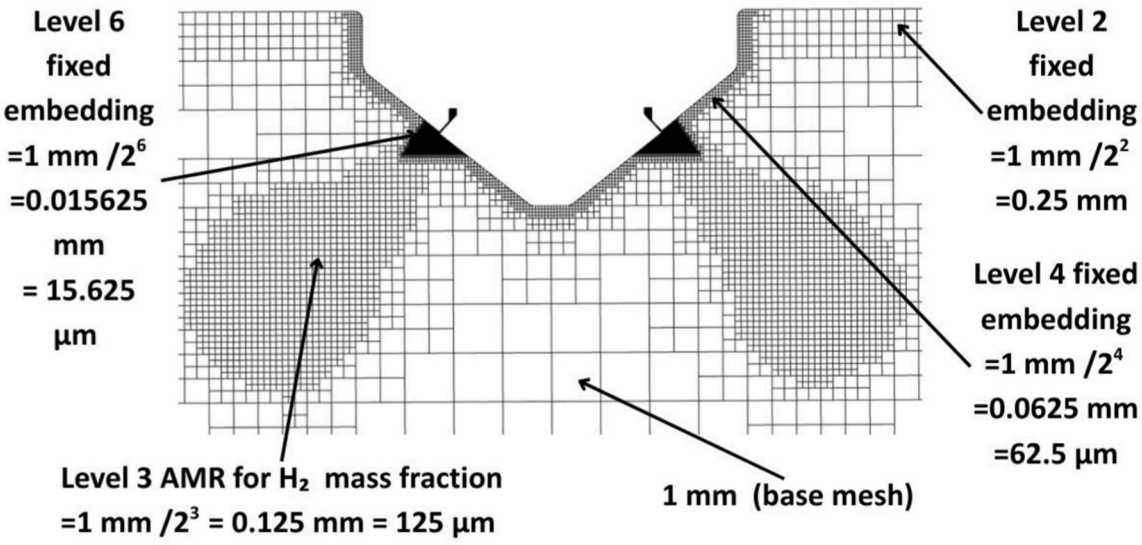

c)Meshing strategies applied to the model

Fig. 1. Constant volume chamber geometry, hollow-cone injector geometry and grid resolution of the domain at t = 0.1 ms.

gasoline direct injection) into a constant volume chamber operated at room temperature and supplied with pure N_2, where the high-speed Schlieren system was employed for the visualisation of hydrogen jets. Image processing is applied to the Schlieren images to detect and trace the contours of density gradients generated by H_2 injection. Data on jet penetration is derived from the analysis of these contours. Specifications of the Bosch HDEV4 hollow cone injector and test conditions for 3D-CFD model validation are presented in Table 2.

The primary reason for selecting a chamber pressure of 2 bar was to strictly follow the experimental test conditions for numerical model validation. In addition, when considering a low-pressure injection which actually more suitable for very early/early injection of H_2 into to the internal combustion engine, a chamber pressure of 2 bar represents a practically realistic test condition.

Also, sensitivity analysis of CFD model parameters such as mesh resolution, CFL number, Sc_t, number, and URANS turbulence models is discussed, and their influence on predicting H_2 jet penetration is analysed in Fig. 2. In the validation and sensitivity studies, the geometry was initially divided into two distinct regions: the chamber region, which encompasses all constant-volume chamber surfaces, and the

Table 2
Bosch HDEV4 injector specification and test conditions for model validation [39, 48].

Hollow Cone Injector Specifications	
Needle actuation	Direct outward-opening piezo injector
Spray angle	85°
Needle lift	35 μm
System pressure	20 MPa
Droplet size SMD	10-15 μm
Injection time	70-5000 μs
Metering range	0.5-150 mg/injection
Test Conditions	
Injection pressure	51 bar
Chamber pressure	2 bar
Pressure ratio	25.5
Temperature	300 K
Ambient gas	N_2
Mass flow rate	0.93 mg/ms
Simulation duration	1 ms

injector region, which includes all injector surfaces. A total of three boundary-condition groups were established: wall, inflow, and outflow. The surface indicates as the injector inlet in Fig. 1b is designated as the inflow boundary condition, while the lateral and inferior surfaces of the constant-volume chamber are classified as outflow boundaries. These surfaces allow fuel to escape, reducing pressure build-up within the chamber. Inlet boundary was treated as an inflow with a total pressure of 51 bar, a pressure boundary condition, with zero normal gradient velocity boundary condition, with H_2 mass fraction sum of 1 species boundary condition, with 0.01 intensity turbulent kinetic energy boundary condition, and with 3e-05 length scale turbulent dissipation boundary condition. Lateral and interior surfaces of the constant-volume chamber were treated as an outflow with a static pressure of 2 bar as a pressure boundary condition, with a zero normal gradient velocity boundary condition. The law-of-the-wall velocity boundary condition was defined on the remaining surfaces. Fixed temperature boundary conditions were set to 300 K for all wall surfaces and the inlet. The boundary conditions applied in the simulation are given in Table 3.

The initial conditions are as follows: the previously mentioned chamber and injector regions are set to initial pressures of 2 bar and 51 bar, respectively, with an initial mass fraction of 1 for the N_2 and H_2 species. There is no cross-flow inside the chamber; solely free stream occurs.

Additionally, both regions were initialised with an initial temperature of 300K, 1 m^2/s^2 turbulent kinetic energy, and 100 m^2/s^3 turbulent dissipation. The initial conditions applied in the simulation are given in Table 4.

2.4.1. Numerical mesh

The examination of mesh sensitivity uses three base mesh sizes: coarse (1.25 mm), medium (1 mm), and fine (0.85 mm). All other mesh refinement strategies were consistently applied across the three scenarios. The model validation is performed using experimental data in Ref. [39]. Penetration length was measured from the injector tip to the boundary of a 0.001 hydrogen mass fraction iso-contour, following the recommendations by ECN [49]. Fig. 2a illustrates the temporal variation in the axial penetration of the hydrogen jet produced by the hollow-cone injector, with three distinct mesh resolutions.

The three distinct mesh configurations produce equivalent penetration at the early stage. After 0.1 ms, the coarse mesh configuration consistently overestimates H_2 penetration throughout the injection phase. This results from insufficient mesh refinement at the injector outlet. Analysis of the medium and fine mesh configuration indicates minor discrepancies; however, penetration data up to 0.8 ms demonstrates a generally favourable correlation with experimental data, where the medium mesh configuration achieves an optimal balance between accuracy and computational expenses.

2.4.2. CFL number

The CFL number constitutes a dimensionless parameter that is essential in numerical simulations. This number defines a correlation among the time step size, spatial grid size, and flow velocity, acting as a determinant of the stability of the simulation process.

CFL number can be calculated using the following formula:

$$CFL = \frac{u\,\Delta t}{\Delta x} \tag{5}$$

Where u is the flow velocity, Δt is the time step size and, Δx is the grid size. Several studies in the current literature have suggested various values for the CFL number. Cabezas et al. [39] and Pucillo et al. [25] advocate a CFL number of 1 in combination with the RANS k-ε turbulence model. In contrast, the study by Fleischmann et al. [35] indicates a CFL number of 10 for RANS simulations using the same turbulence model and a CFL number of 1 for LES. Also, the study of Tang et al. [36] utilised a CFL number of 0.65 for the LES model. Three distinct CFL numbers (0.5, 1, and 5) were evaluated with a medium mesh configuration for the current model. In this comparative analysis, all parameters apart from the CFL number are kept the same.

Fig. 2b demonstrates the effect of CFL number on the H_2 axial jet penetration. Results align with the experimental data in the initial phase of the simulation, but the deviation becomes slightly visible after 0.6 ms. It has been shown that an increase in the CFL number results in an overprediction of H_2 jet penetration length, where maximum penetration is observed at a CFL number of 5. The evaluation of scenarios with CFL numbers of 1 and 0.5 supports the findings of Fleischmann et al. [35], indicating that a decrease in the CFL number improves the temporal resolution of flow variables. Upon comparison of the CFL numbers of 1 and 0.5 cases, it is apparent that they yielded very similar outcomes. Hence in this study, a CFL number of 1 is identified as the most favourable in terms of computational cost.

2.4.3. Turbulent schmidt number

The turbulent Schmidt number is a dimensionless metric that quantitatively represents the ratio of turbulent momentum diffusivity, or eddy viscosity, to turbulent mass diffusivity, also known as scalar diffusivity [50]. The turbulent Schmidt number can be calculated via the following formula.

$$Sc_t = \frac{\nu_t}{D_t} \tag{6}$$

where ν_t is the turbulent kinematic viscosity and D_t is the turbulent molecular diffusivity. This parameter indicates the relative importance of momentum diffusivity compared to mass diffusivity, especially in the context of turbulence analysis. According to previous studies, the Sc_t value varies between 0.2 and 0.78 [51]. To determine the ideal value for the Sc_t, four different values: 0.2, 0.3, 0.56, and 0.78, were tested using a medium mesh. Fig. 2c depicts the effect of Sc_t on H_2 jet penetration and compares the findings with experimental data. It demonstrates that, up to 0.25 ms, all cases yield nearly identical results that correspond closely with the experimental data. This observation indicates that the impact of the Sc_t number is limited during the initial phase of injection, aligning with the results reported by Scarcelli et al. [52]. In the current work, observations indicated that after approximately 0.6 ms, the 0.78 Sc_t case exhibited an overprediction in penetration. When Sc_t values were decreased to 0.56 and 0.3, the results aligned more closely with the experimental findings. Nonetheless, further reduction of Sc_t to 0.2 resulted in fluctuations when compared to the cases of 0.56 and 0.3. In addition, H_2 mass fraction iso-surface volumes for different turbulent Schmidt number cases are presented in Fig. 3.

It shows that the reduction of Sc_t enhances fuel distribution, facilitated by the greater radial penetration and leading to an increase in the total volume of the H_2 mass fraction iso-surfaces, aligning the results more closely with experimental data; however, no beneficial effect was

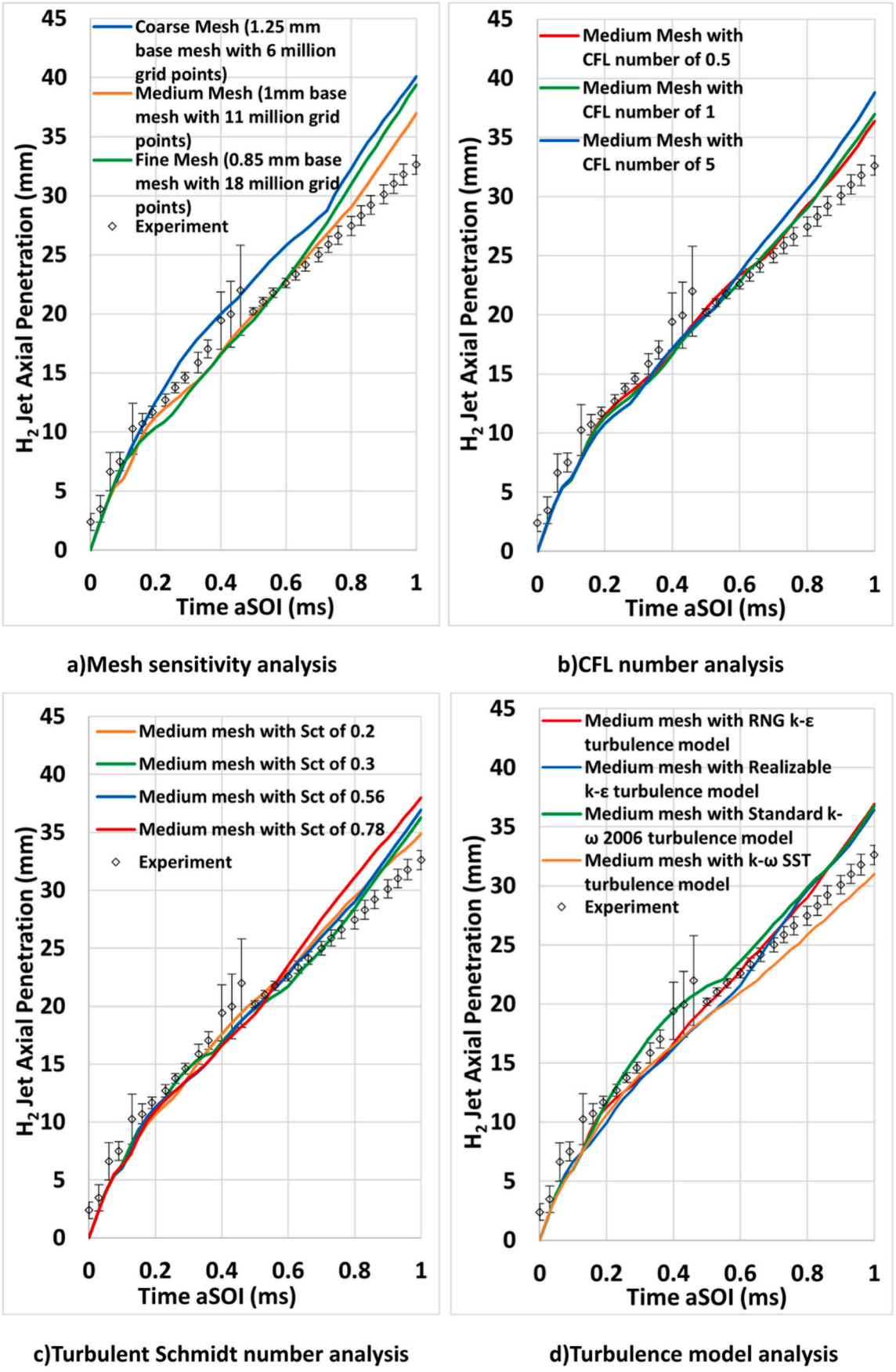

Fig. 2. Mesh sensitivity, CFL number, turbulent Schmidt number and turbulence model analysis.

Table 3
Boundary conditions applied in the simulation.

Boundary Type	Pressure	Velocity	Temperature	Species	Turbulent kinetic energy	Turbulent dissipation
Inflow	51 bar total pressure	Zero normal gradient	300 K	H_2 mass fraction sum = 1	Intensity = 0.01	Length scale = 3e-05
Outflow	2 bar static pressure	Zero normal gradient	300 K	-	-	-
Wall	-	Stationary fixed wall	Law of the wall(300 K)	-	-	-

Table 4
Initial conditions applied in the simulation.

Region Type	Pressure	Velocity	Temperature	Species	Turbulent kinetic energy	Turbulent dissipation
Chamber	2 bar	0 m/s	300 K	N_2 mass fraction sum = 1	1 m^2/s^2	100 m^2/s^3
Injector	51 bar	0 m/s	300 K	H_2 mass fraction sum = 1	1 m^2/s^2	100 m^2/s^3

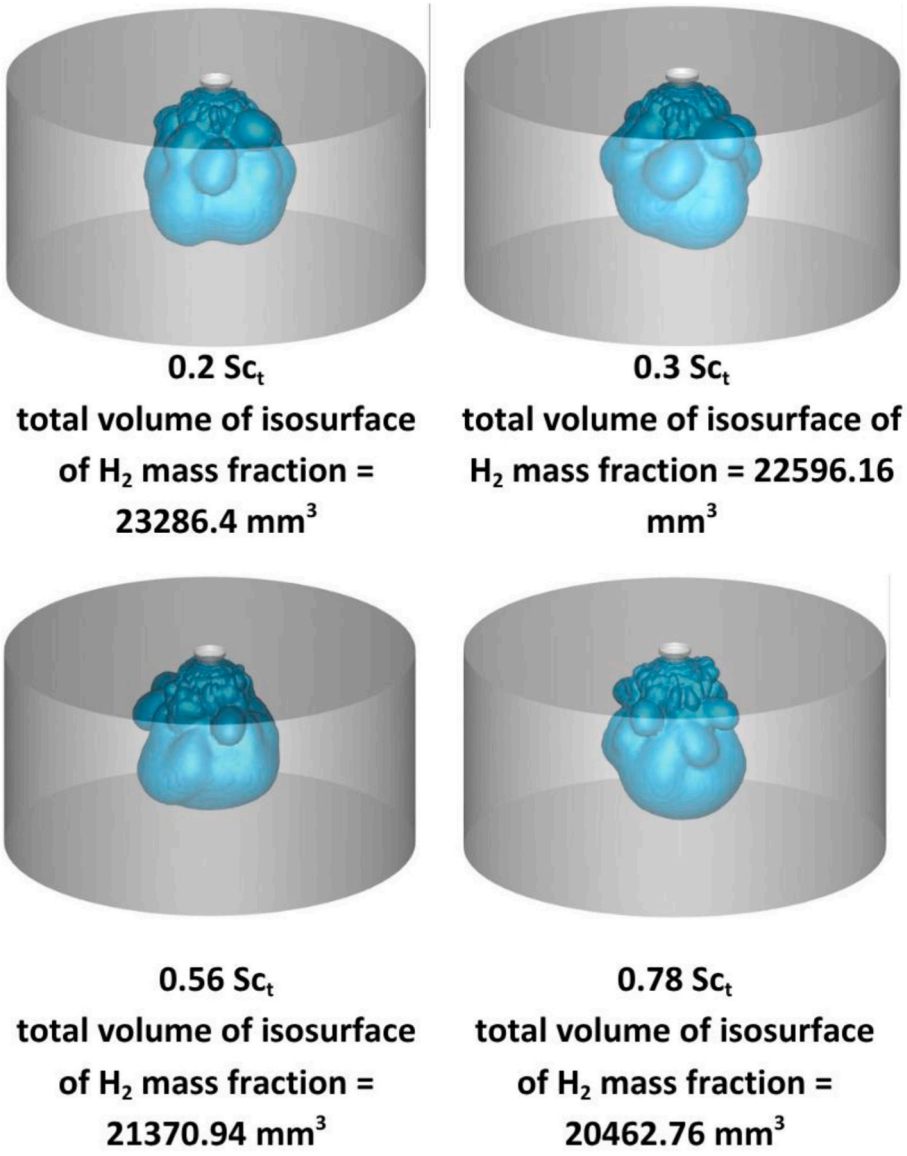

Fig. 3. Effect of turbulent Schmidt number on H_2 mass fraction iso-surface volume.

noted when Sc_t was further decreased to 0.2. The optimal range for Sc_t is established between 0.3 and 0.56. As a result, Sc_t value of 0.56 was selected for all simulations to be presented in subsequent stages of the study due to its consistency with the experimental results.

2.4.4. URANS turbulence model

Fig. 2d demonstrates the effect of four different URANS turbulence models, namely, RNG k-ε, realizable k-ε, standard k-ω 2006, and k-ω shear stress transport (SST), on the H_2 jet penetration and compares these models with experimental results. The discrepancies in the predictions of the four turbulence models are directly associated with the

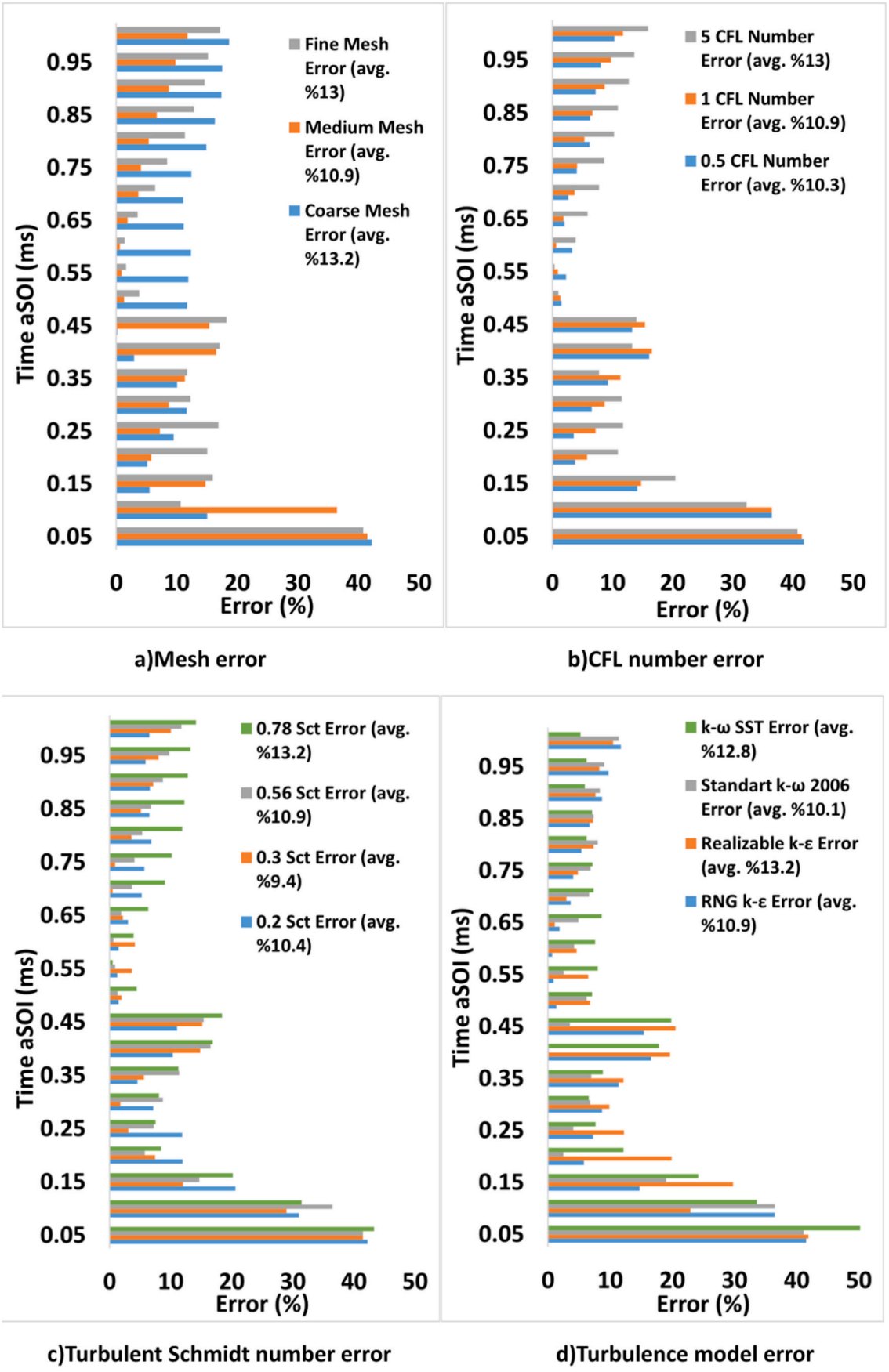

Fig. 4. Error analysis of the CFD model parameters.

formulations. The RNG k-ε model enhances strain-rate sensitivity and swirl control via its renormalization-group correction, making it especially advantageous for high-shear, hollow-cone injection. Consequently, it produced axial penetration values that aligned most closely with the experimental data, especially within the region of 0.1 to 0.7 ms. The realizable k-ε model improves the representation of Reynolds stresses and more precisely characterises jet dispersion in free-shear areas. This enhancement is seen in its robust correlation with measurements, while a little underprediction is noted at the mid-injection period. The standard k-ω 2006 model has considerable sensitivity to near-wall turbulence, often leading to increased dissipation in free-jet regions, hence intensifying turbulent mixing. As a result, it always forecasts the highest axial penetration and exhibits the most significant overestimation during the whole injection duration. The k-ω SST model combines the free-stream attributes of the k-ε model with the near-wall accuracy of the k-ω model, but the blending of the two can often result in enhanced damping in the outer jet area, yielding the lowest penetration estimates and a persistent underestimation of experimental data.

2.4.5. Error analysis of the CFD model parameters

Additionally, a quantitative error analysis was carried out to quantify CFD modelling errors with respect to different CFD model parameters. As defined in Eq. (7), the mean absolute percentage error (MAPE) was selected as a quantitative error metric.

$$MAPE\ (\%) = 100\ \frac{1}{n}\sum_{t=1}^{n}\left|\frac{A_t - F_t}{A_t}\right| \tag{7}$$

where A_t is the experimental value, F_t is the forecast value, and n is the number of fitted points. Error analysis of CFD parameters is presented in Fig. 4. The mesh sensitivity error analysis reveals MAPE values of around 13% for the coarse and fine mesh and 10.9% for the medium mesh, which demonstrates the closest alignment with the experimental data. While CFL number 5 exhibits the largest error with a MAPE of 13%, CFL numbers 1 and 0.5 show comparable errors of 10%, with CFL number 1 distinguished by its computational efficiency. With an approximate MAPE of 10%, the optimal Sc_t range is determined to be between 0.56 and 0.3. The analysis of turbulence models indicates that the realizable k-ε and k-ω SST models presented the greatest errors, with MAPEs of 13.2% and 12.8%, respectively. The standard k-ω 2006 model demonstrates a 10.1% error, outperforming the RNG k-ε model with a 10.9% MAPE. However, this performance is attributed to the standard k-ω 2006 model's overestimation in the 0.3–0.6 ms range, where experimental results exhibit a broad distribution. Therefore, the RNG k-ε model is evident as an optimal turbulence model following the error analysis.

3. Results and discussions

This section provides 3D-CFD results for the low-pressure H_2DI strategy and its mixing characteristics for the hollow cone injector geometry in a constant-volume chamber under engine-relevant conditions. Results are presented in two separate sections: local flow dynamics, mixing characteristics, and turbulence development for a hollow-cone injector, first by varying the injection pressures while maintaining a constant chamber pressure, then by varying the injector's needle lift and injection pressure while maintaining a constant chamber pressure and total injected fuel mass.

3.1. Analysis of local flow, mixing characteristics and turbulence formation for the hollow-cone injector with varying injection pressure and needle lift with fixed chamber pressure

This section examines the impact of varying the injection pressure to 20.7, 51, and 100 bar on local flow dynamics, mixing characteristics, and turbulence formation while maintaining a constant chamber pressure of 2 bar across both 35 and 85 μm needle lift scenarios. Simulation conditions are given in Table 5.

Table 5
Simulation conditions with varying injection pressure and needle lift with fixed chamber pressure.

Test cases	Needle lift	Injection pressure	Chamber pressure	Total Injected Fuel	Total grid resolution
1	35 μm	100 bar	2 bar	1.82 mg	17.3 million
2	35 μm	51 bar	2 bar	0.93 mg	11 million
3	35 μm	20.7 bar	2 bar	0.37 mg	6.94 million
4	85 μm	100 bar	2 bar	4.49 mg	29.9 million
5	85 μm	51 bar	2 bar	2.30 mg	19.9 million
6	85 μm	20.7 bar	2 bar	0.93 mg	12.5 million

Here, the influence of injection pressure and needle lift on jet morphology was examined through an analysis of total injected fuel mass, axial and radial jet penetration, and the associated turbulent kinetic energy. Fig. 5 illustrates the impact of varying injection pressures on the total injected mass and H_2 jet axial penetration, maintaining a constant chamber pressure across two needle lift scenarios.

The results presented in Fig. 5a indicate that an elevation in injection pressure, while maintaining a constant chamber pressure, is associated with a larger amount of fuel exiting the nozzle because of increased jet velocity and momentum. Also, raising the needle lift from 35 μm to 85 μm increases the effective hydraulic flow area, and a larger flow area decreases hydraulic resistance, enabling more fuel to pass through the injector. This explains the consistent increase in total injected mass as needle lift values are elevated at the same injection and chamber pressures.

The effect of varying injection pressure on axial and radial jet penetration when chamber pressure is fixed at 2 bar is shown in Figs. 5b and 6a, respectively, across two needle lift scenarios.

Axial and radial jet penetration at different injection pressures demonstrate an initial overlap in the early stages. Subsequently, the penetration profiles displayed a division, following approximately linear trajectories for axial penetration, while radial penetration exhibits fluctuations throughout and a levelling out after an initial fast ramp-up. It is clearly observed that an increase in injection pressure results in a proportional enhancement of both penetration types, which aligns with the various studies [23–25,27,29]. The observed phenomenon is attributable to the enhancement of jet momentum, alongside an increase in the total injected fuel mass, which correlates directly with the increase in injection pressure.

It is observed that an increase in injection pressure leads to a pronounced dispersion of the jet in the radial direction, while the effect on axial penetration is considerable but slightly less in comparison to the radial spreading. For example, the elevation of injection pressure from 20.7 bar to 51 bar and subsequently to 100 bar in a 35 μm needle lift case resulted in a notable enhancement in axial penetration, which increased by 23% and 52%, respectively, at the end of the injection. Concurrently, radial penetration exhibited a significant increase, demonstrating an approximate 28% and 68% enhancement, respectively. Increasing the needle lift from 35 μm to 85 μm resulted in a 22%, 13%, and 11% increase in axial penetration for the NPR cases of 10.35, 25.5, and 50, respectively. Conversely, radial penetration exhibited increases of 30%, 46%, and 26% for the same NPR cases. The elevation in needle lift indicates that the expansion of the effective flow area amplifies the propensity of the injected fuel to disperse radially more significantly than in the axial direction. The increased flow area leads to a more robust and less restricted jet, which is characterised by enhanced radial expansion.

Additionally, the effect of varying injection pressure on mass-averaged turbulent kinetic energy when chamber pressure is fixed at 2 bar is illustrated in Fig. 6b across two needle lift scenarios. As a general trend, elevated turbulent kinetic energy is observed when the injection pressure and needle lift are increased. Elevated injection pressure and

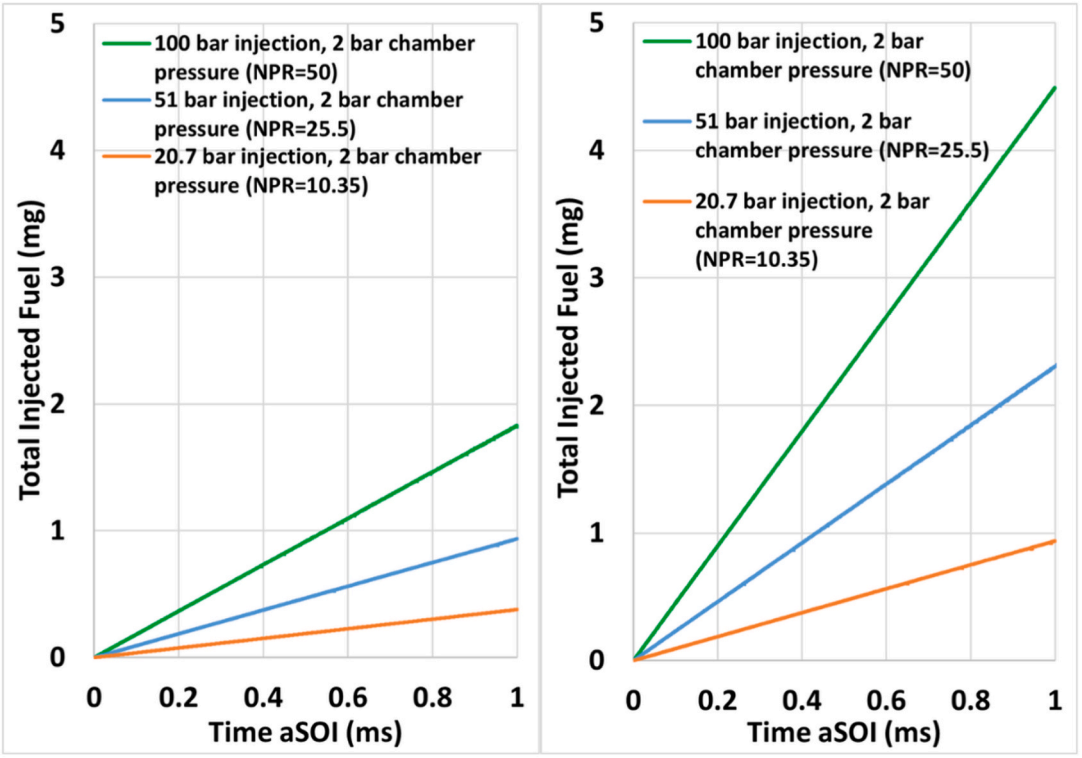

a)Effect of injection pressure on total injected fuel mass with fixed chamber pressure : 35 µm needle lift (left), 85µm needle lift(right)

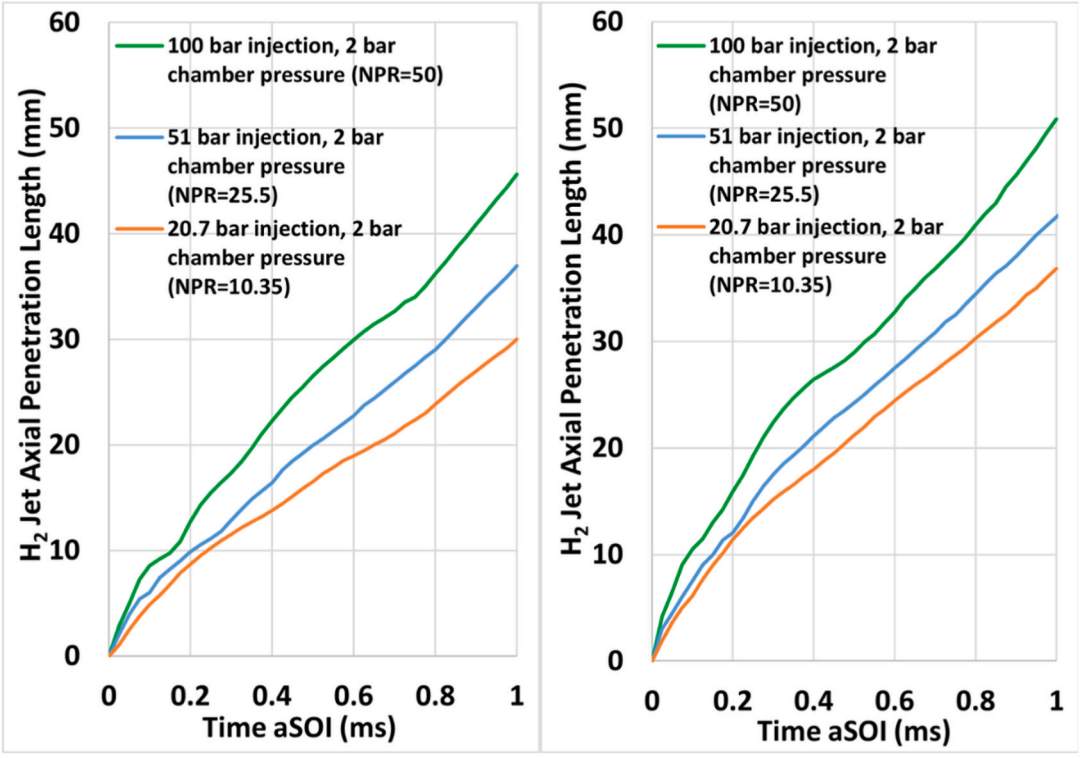

b)Effect of injection pressure on H_2 jet axial penetration with fixed chamber pressure: 35 µm needle lift (left), 85µm needle lift (right)

Fig. 5. Effect of injection pressure on total injected fuel mass and H_2 jet axial penetration.

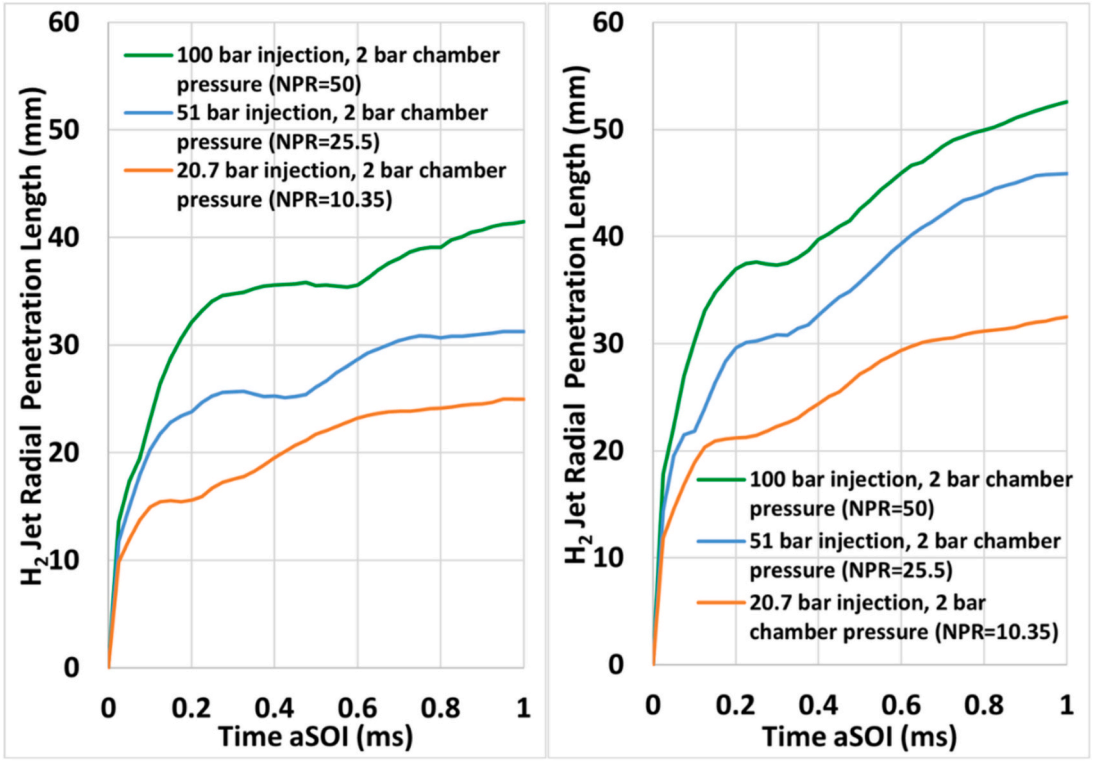

a)Effect of injection pressure on H_2 jet radial penetration with fixed chamber pressure: 35 µm needle lift (left), 85µm needle lift (right)

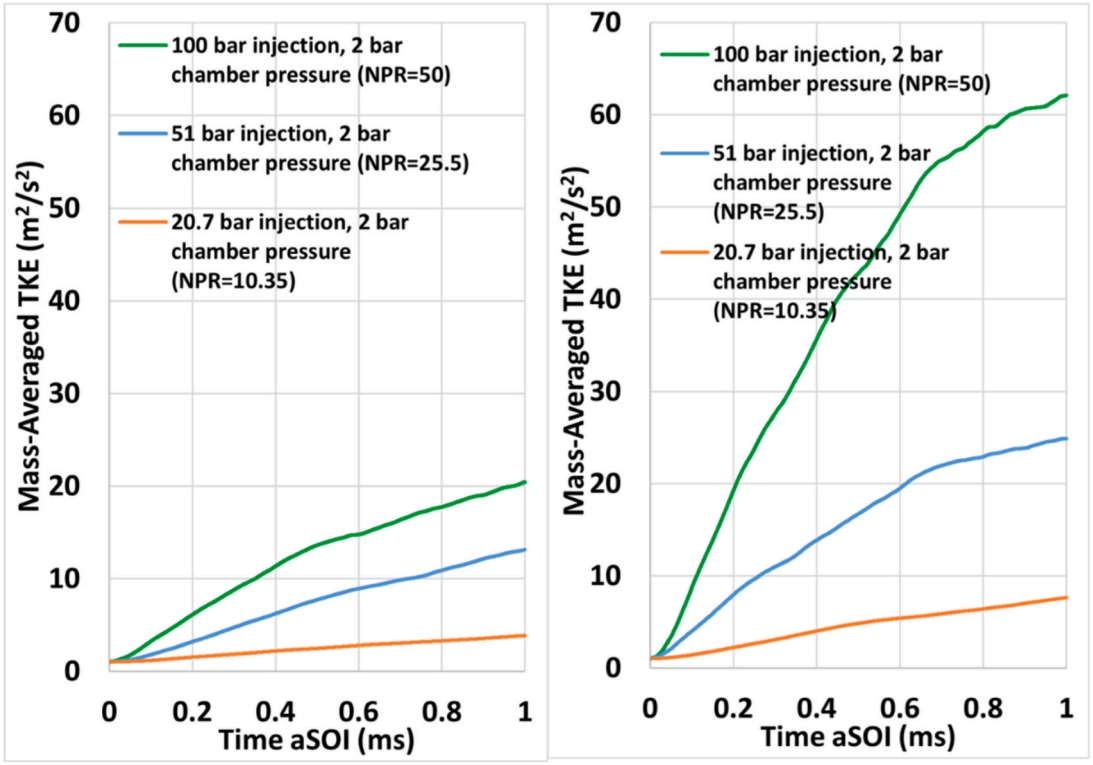

b)Effect of injection pressure on on mass-averaged TKE with fixed chamber pressure: 35 µm needle lift (left), 85µm needle lift (right)

Fig. 6. Effect of injection pressure on H_2 jet radial penetration and mass-averaged TKE.

Table 6
Simulation conditions with varying injection pressure and needle lift with fixed chamber pressure and total injected fuel.

Test case	Needle lift (μm)	Injection pressure (bar)	Chamber pressure (bar)	Mass flow rate (mg/ms)	Injection duration (ms)	Injected fuel (mg)	Grid resolution (in million)
1	35	51	2	0.93	1	0.93	11
2	85	20.7	2	0.93	1	0.93	12.5
3	135	12.68	2	0.93	1	0.93	12.1

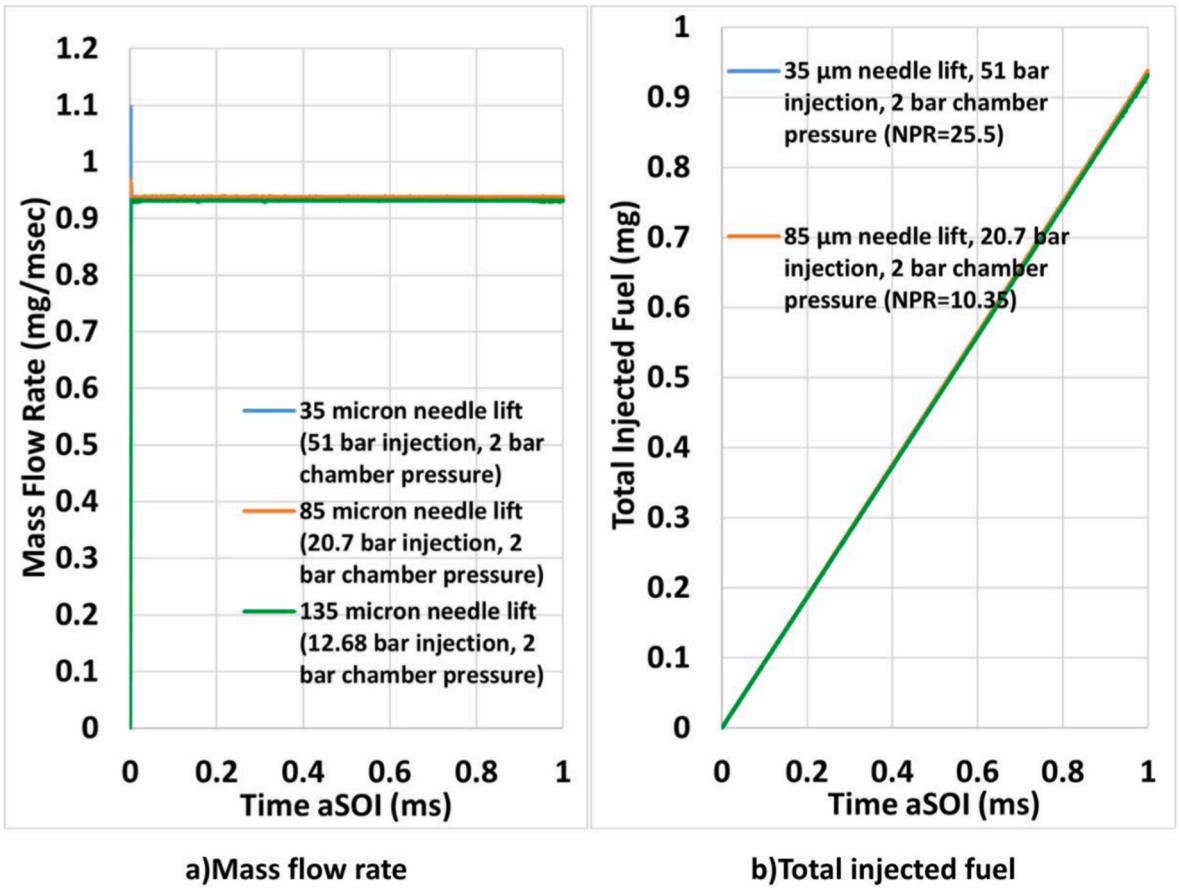

Fig. 7. Fixed total injected fuel mass for 35 μm, 85 μm and 135 μm needle lift configurations.

needle lift lead to a substantial increase in fuel mass flow through the nozzle, consequently enhancing the jet exit velocity and momentum flux. The augmentation of jet momentum enhances velocity gradients at both the nozzle exit and the jet boundary, facilitating the development of larger shear layers, optimising vortex formation, and elevating the generation of small-scale turbulence. Furthermore, the higher pressure drop across the injector can trigger flow instabilities and intensify breakup dynamics, both of which contribute to an accelerated generation of turbulence. At 35 μm, increasing the nozzle pressure ratio (NPR) from 10.35 to 25.5 and 50, respectively, resulted in an elevation of turbulent kinetic energy from 3.87 m^2/s^2 to 13.13 and 20.44 m^2/s^2 at 1 ms after the start of the injection (aSOI), a nearly twofold increase at each respective NPR. While at 85 μm, turbulent kinetic energy increased from 7.67 m^2/s^2 to 24.87 and 62.10 m^2/s^2, respectively, experiencing a roughly threefold increase at each respective stage. The findings highlight the critical role of injection pressure and needle lift in modulating turbulence formation through their influence on mass flow rate, jet velocity, and momentum.

3.2. Analysis of local flow, mixing characteristics and turbulence formation of the hollow-cone injector with constant total injected fuel mass

This section examines the impact of modifying nozzle exit area (by altering needle lift) and injection pressure on local flow dynamics, mixing characteristics, and turbulence generation while maintaining a constant total injected fuel mass. In this section, the mass flow rate of 0.93 mg/ms across all three configurations is analysed. The total amount of fuel injected is held constant at 0.93 mg, which corresponds to an injection duration of 1 ms. Since the nozzle outlet areas and injection pressures were adjusted to ensure that the same total amount of fuel is delivered at a constant mass flow rate over the same injection duration, a fixed injection duration of 1 ms was applied in all simulations Here numerical simulations were performed utilising controlled injection pressures of 51 bar, 20.7 bar, and 12.68 bar for the cases of 35 μm, 85 μm, and 135 μm needle lift, respectively, with a constant chamber pressure of 2 bar across all cases. Simulation conditions are given in Table 6.

The injection pressure for each scenario was calculated utilising Eq. (8) presented below [53]. This methodology guarantees the stability of the mass flow rate and the cumulative mass of fuel injected, despite alterations in the needle lift.

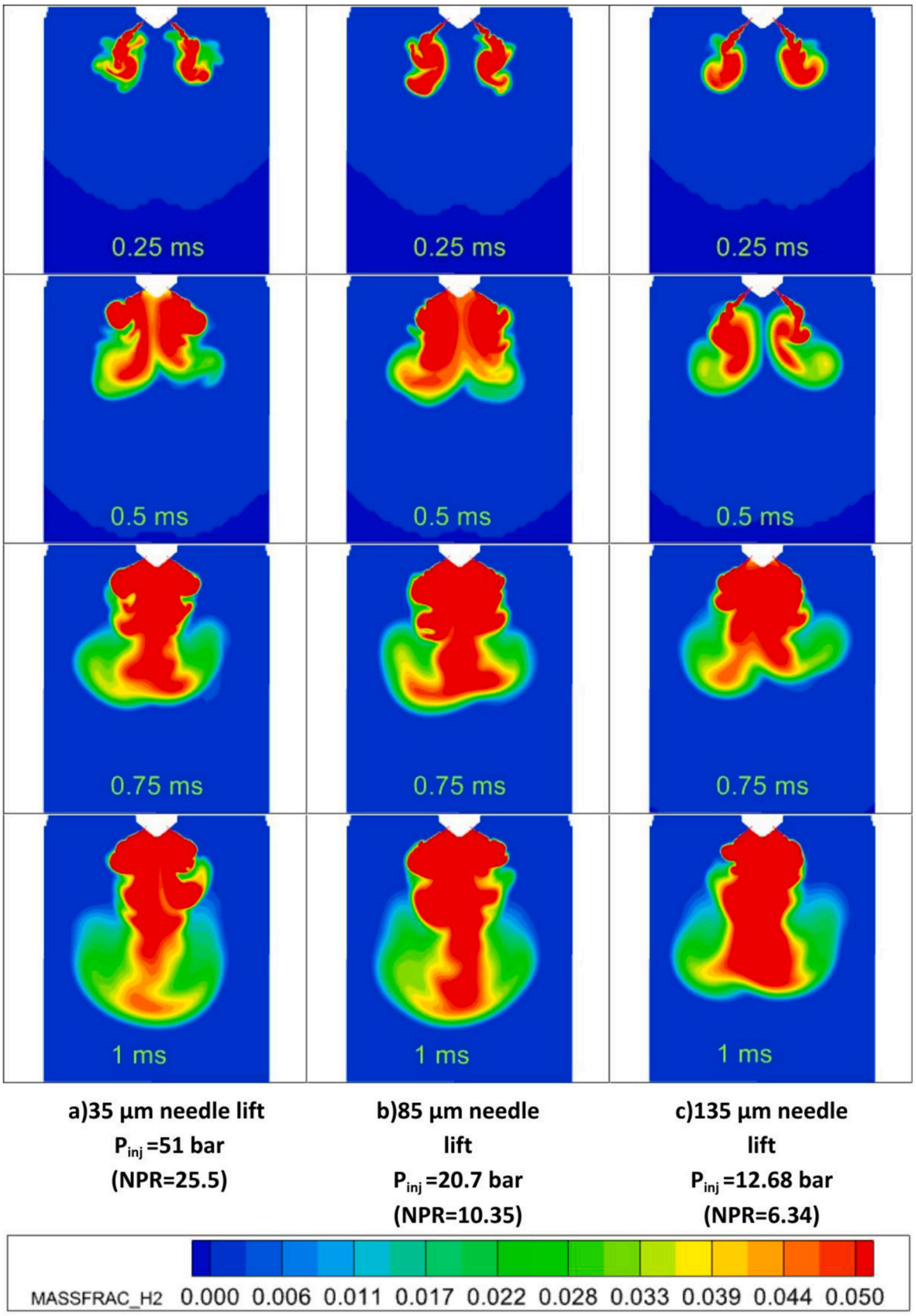

Fig. 8. Hydrogen mass fraction contour development in a midplane for different needle lift configurations.

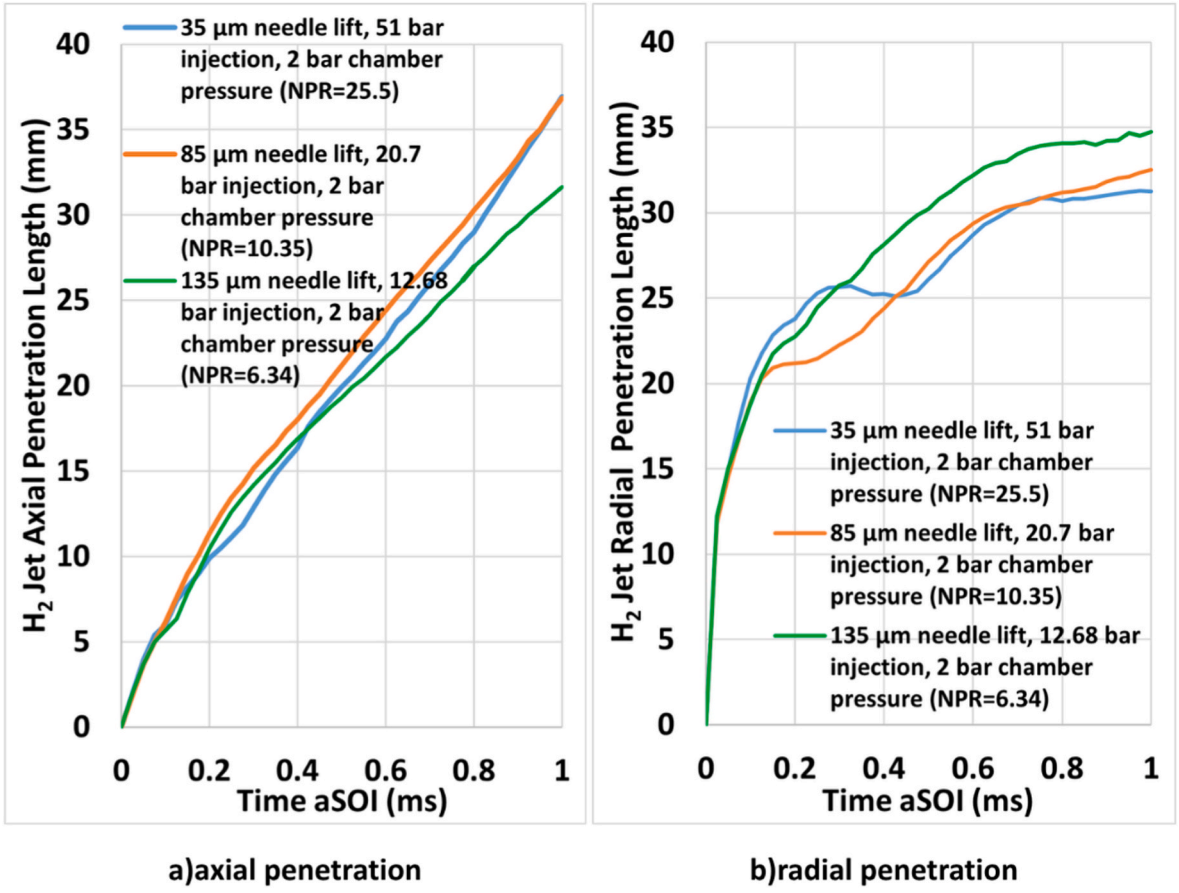

Fig. 9. Effect of needle lift on axial and radial penetration of H_2 when the total injected fuel mass is fixed.

$$\dot{m}_{theory} = A_e\, P_i \sqrt{\frac{\gamma}{RT}} \left(\frac{\gamma+1}{2}\right)^{\frac{\gamma+1}{2(1-\gamma)}} \tag{8}$$

where $\dot{m}_{theory}$ is the theoretical mass flow rate, A_e is the area of the nozzle exit, P_i is the injection pressure, γ is the specific heat ratio, R is the gas constant, and T is the temperature.

The implementation of Eq. (8) produced injection pressure values of 51 bar, 20.7 bar, and 12.68 bar for the respective conditions of 35 µm, 85 µm, and 135 µm. In contrast to the preceding section, this section maintains a constant total fuel injection amount by decreasing the injection pressure as the needle lift is increased. Since increasing the needle lift increases the nozzle exit area, the injection pressure has been reduced to maintain a constant mass flow rate. Fig. 7 shows constant mass flow rate and total injected fuel for three different needle lift configurations.

To better analyse the effect of needle lift and injection pressure on the mixing performance, H_2 mass fraction contour development in a midplane for different needle lift configurations is illustrated in Fig. 8. In the 135 µm needle lift scenario, a lower injection pressure of 12.2 bar leads to the formation of a jet characterised by a comparatively low velocity and reduced axial momentum. This phenomenon limits axial penetration while concurrently facilitating a wider jet formation, leading to improved radial penetration as a result of enhanced lateral dispersion. In the 35 µm needle lift scenario, a higher injection pressure of 51 bar leads to the production of increased jet velocities. The significant throttling effect at the nozzle results in higher turbulence, which yields a moderate level of axial and radial penetration relative to the other scenarios. The 85 µm needle lift and 20.7 bar injection pressure case achieves sufficient velocity and momentum while concurrently minimising excessive restriction in the nozzle, resulting in maximum axial penetration and minimum radial penetration, attributable to the jet's capacity to sustain a more focused trajectory and be less prone to lateral dispersion. The interplay between velocity, flow area, turbulence, and breakup dynamics clarifies the penetration trends noted in axial and radial directions.

The impact of needle lift on the axial and radial penetration while maintaining a constant total injected fuel mass is quantitatively analysed and illustrated in Fig. 9. Firstly, during the very early phase of the injection, the axial and radial penetration values in all three scenarios align up to 0.1 ms. Furthermore, the 85 µm needle lift scenario consistently demonstrates the greatest axial penetration, achieving a depth of 37 mm at the end of injection. 35 µm needle lift scenario demonstrates the least axial penetration during the initial phase of injection, attributable to the influence of significant jet momentum and turbulence. However, it attains the same penetration depth as the 85 µm scenario at 1 ms. The examination of radial penetration reveals a similar trend in the opposite direction. The 35 µm scenario exhibits superior radial penetration compared to the 85 µm scenario until the halfway point of the injection, with both scenarios achieving approximately 32 mm by the end of the injection process. The 135 µm case exhibits both axial and radial penetration between the other scenarios until the midpoint of the injection, while it demonstrates the lowest axial penetration and highest radial penetration at the end of the injection. While the scenario with 85 µm needle lift and 20.7 bar injection pressure demonstrates the best results for axial jet penetration, the scenario with 135 µm needle lift and 12.68 bar injection pressure shows optimal results for radial jet penetration. To further analyse the mixing characteristics, we will now study the H_2 mass fraction distribution and its behaviour within a shear layer region, vorticity characteristics, and turbulent kinetic energies.

Figs. 10 and 11 show radial spreading of three different needle lift scenarios along the jet axis and along the injector central axis,

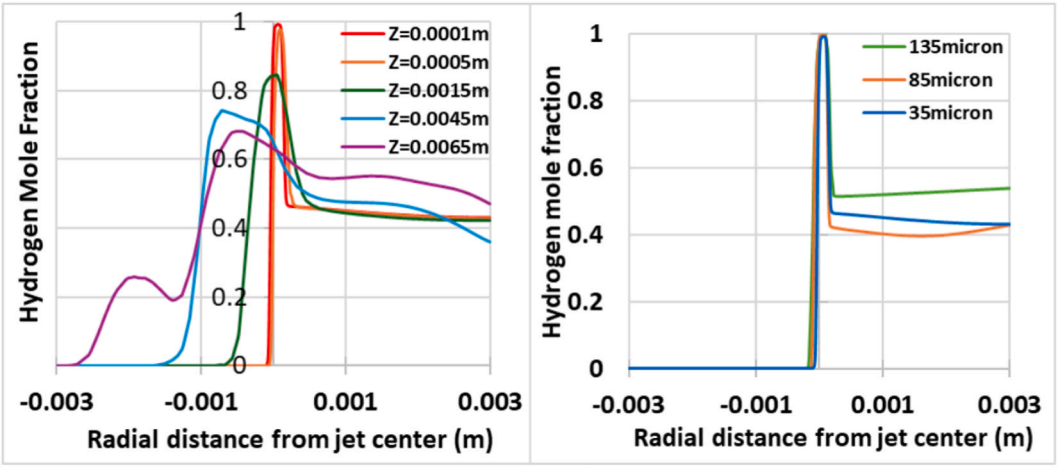

a)Radial spreading at 1ms for the 35 micron needle lift at varying distances downstream of the jet axis

d)Radial spreading at 1ms for varying needle Lift at 0.0001m downstream of the jet axis

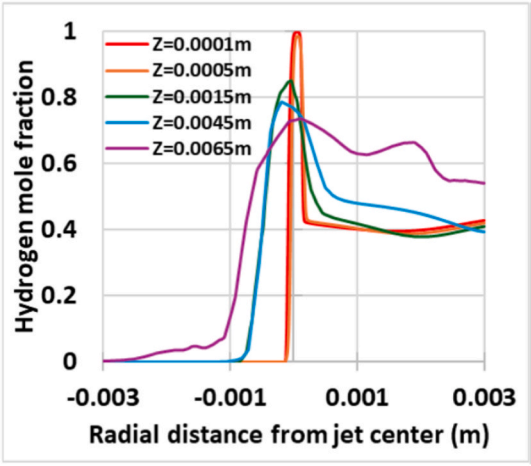

b)Radial spreading at 1ms for the 85 micron needle lift at varying distances downstream of the jet axis

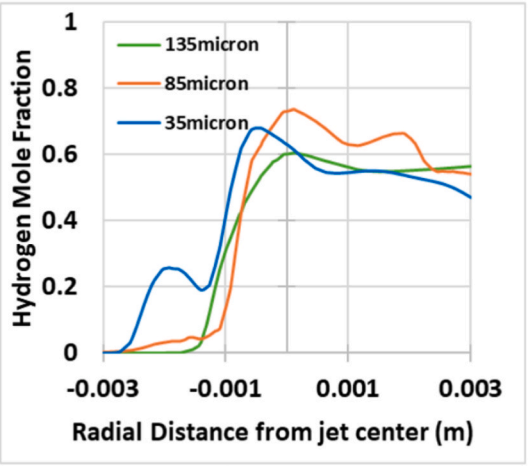

e)Radial spreading at 1ms for varying needle Lift at 0.0065m downstream of the jet axis

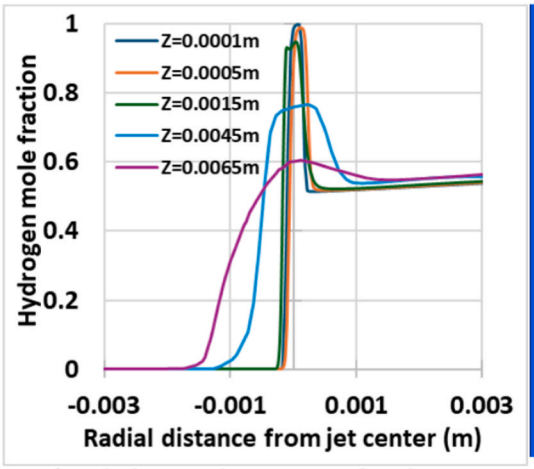

c)Radial spreading at 1ms for the 135 micron needle lift at varying distances downstream of the jet axis

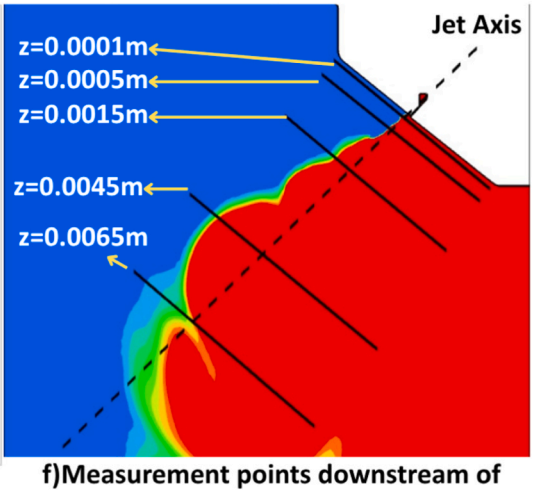

f)Measurement points downstream of the jet axis

Fig. 10. Radial spreading of three different needle lift scenarios along the jet axis.

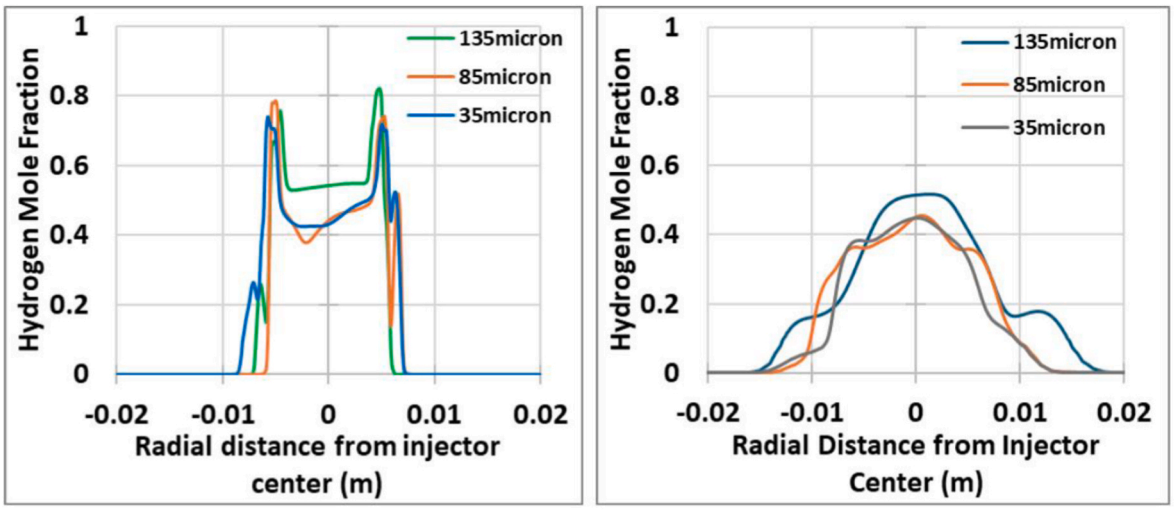

a)Radial spreading at 1ms for varying needle Lift at 0.001m downstream of the injector central axis

b)Radial spreading at 1ms for varying needle Lift at 0.016m downstream of the injector central axis

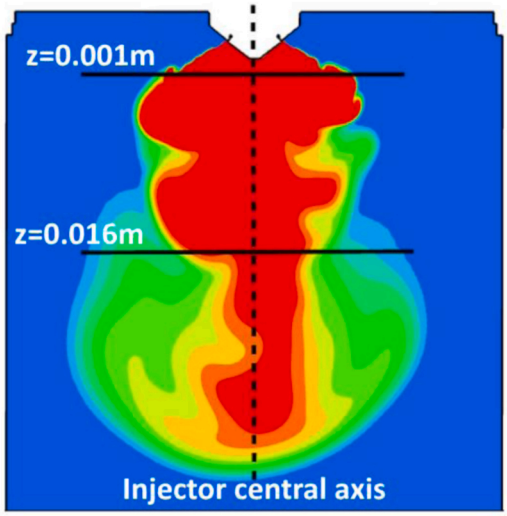

c)Measurement points downstream of the injector central axis

Fig. 11. Radial spreading of three different needle lift scenarios along the injector central axis.

respectively. As seen in Figs. 10 and 11, the areas with a high rate of change of H_2 mole fraction with high velocity gradients indicate shear layer regions for all three test cases. Also, a wider peak indicates a large shear layer for cases with high injection pressure. Furthermore, the vorticity plots in Fig. 12 show the Kelvin-Helmholtz instabilities, which are created along the boundary of the shear layer, which takes momentum from the jet and transfers it to the surrounding bulk, entraining air with the jet, until eventually so much momentum is lost that the jet collapses. Figs. 10 and 11 also exhibit two regions: the inner layer region, where the jet collapses towards the centre below the hollow cone injector and entrains a lot of chamber air, and the outer layer region, where H_2 still interacts with the bulk chamber air. Fig. 10 depicts a lower-pressure inner zone that cannot escape through the higher velocity region around it (hollow cone), which creates the multiple shear layers in the cone. Generally, the mass fraction distributions in Fig. 11 show a much richer region in the centre and a less rich one surrounding it. This is evident in the radial slices of the injector axis, where there is a plateau in the centre that falls off and then plateaus before falling off again, where the fall-off regions are the two separate inner and outer hollow cone shear layers. Similarly, the vorticity contours in Fig. 12 show a region in the centre with minimal vorticity, and where vorticity starts to increase again is the inner shear layer, then a region with more vorticity, and the outer layer of that is the outer shear layer.

Vorticity and flow pattern development in a midplane for different needle lift configurations are shown in Fig. 12. During the initial phase of injection, a small but strong toroidal recirculation zone with high vorticity is consistently observed around the injector because of the shear forces acting between the gases within the internal region of the nozzle. In a 35 μm needle lift scenario, the vortical region exhibits a greater width compared to other scenarios because of the elevated injection pressure and the narrowed injector outlet. During the ongoing injection process, a larger yet less intense vortex and recirculation zone develops downstream, located on the outer side, distinguished by a lower vorticity. The initially identified vortical region restricts the transport and mixing of H_2, whereas the subsequent region facilitates the further transport of H_2 and its mixing with the surrounding gas. In

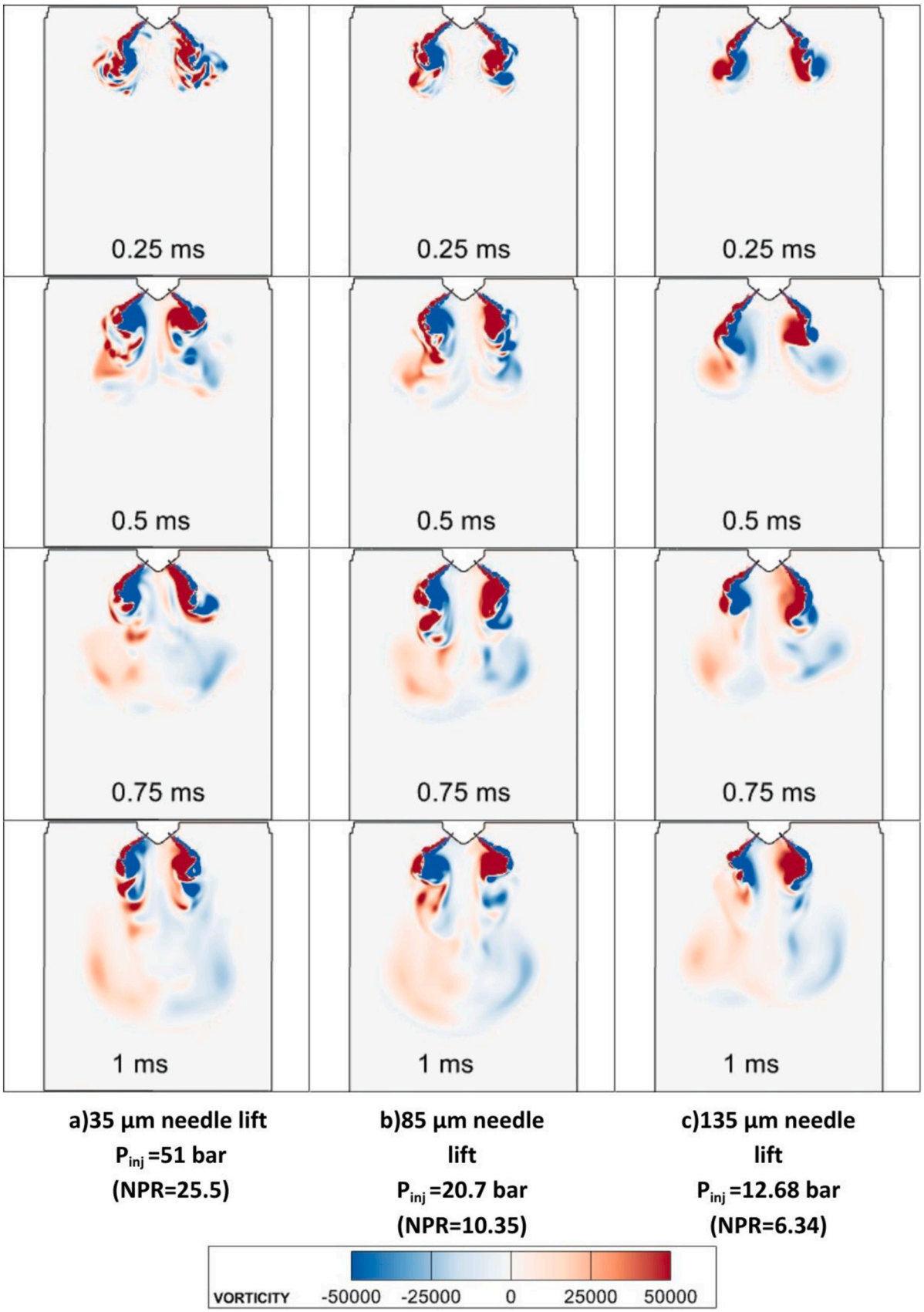

Fig. 12. Vorticity factor and flow patterns development in a midplane for different needle lift configurations.

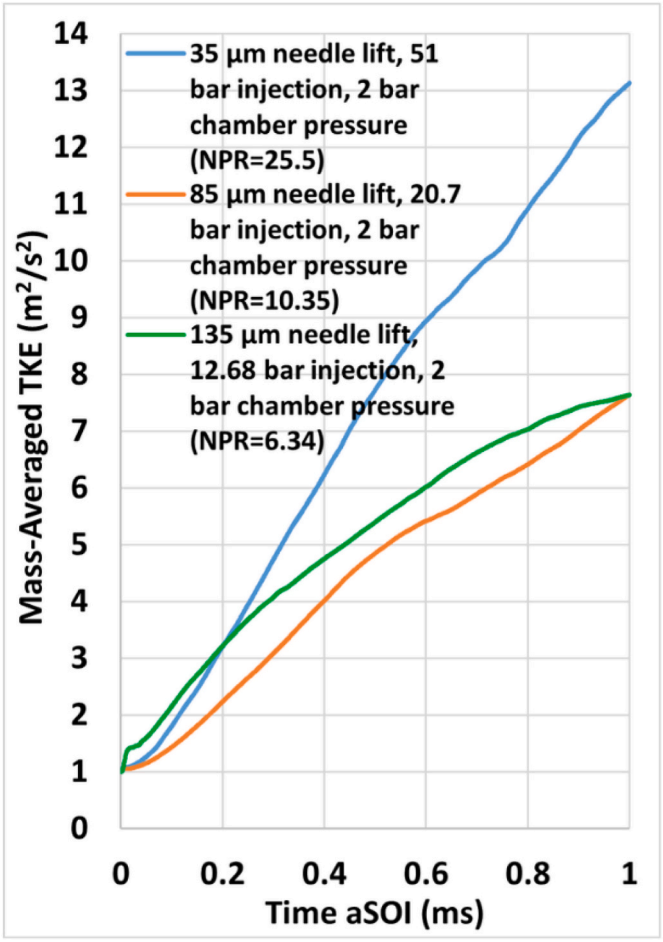

Fig. 13. Effect of needle lift on mass-averaged TKE when total injected fuel mass is fixed.

the middle and later phases of the injection process, it was noted that in the 35 µm needle lift scenario, smaller yet more intense vortex and recirculation zones were replaced by considerably larger but less dense vortex regions. In the remaining two scenarios, the small yet powerful vortex and recirculation regions sustained their effects.

The impact of needle lift and injection pressure on flow patterns and vorticity is associated with the turbulent kinetic energy produced, as illustrated in Fig. 13. The calculated Reynolds numbers based on hollow cone injector diameter (see Fig. 1), nozzle exit velocity, density, and dynamic viscosity for the 35 µmmicron needle lift and 51 bar injection pressure, 85 µmmicron needle lift and 20.7 bar injection pressure, and 135 µm needle lift and 12.68 bar injection pressure cases are 1.12e+05, 1.11e+05, and 0.8e+05 respectively. It can be seen that the 35 µm needle lift and 51 bar injection pressure scenario is characterised by the highest turbulent kinetic energy, around 13 m^2/s^2, at the end of injection, demonstrating pronounced regions of higher vorticity and significant jet momentum, accompanied by strong shear layers. Significant fuel throttling occurs under these circumstances, resulting in very high velocity gradients at the nozzle orifice. Conversely, scenarios characterised by approximately half the turbulent kinetic energy (around 8 m^2/s^2) generate larger vortex regions, although the vortices they create carry less energy. On the other hand, 135 µm needle lift and an injection pressure of 12.2 bar case reduces flow restriction, but jet velocity and momentum are constrained by the comparatively low injection pressure, leading to a moderate turbulent kinetic energy. The lowest turbulent kinetic energy was found in the case with an 85 µm needle lift and an injection pressure of 20.7 bar. This behaviour is explained by the interaction of moderate pressure with needle lift, which produces a more balanced flow with less shear intensity. Because of its slightly larger effective flow area, the observed modest difference in turbulent kinetic energy between the 85 µm and 135 µm situations may be explained. Even at lower pressures, this larger flow area makes it easier to create slightly higher local shear and turbulence.

4. Conclusions

In the present study, three-dimensional unsteady Reynolds-averaged Navier-Stokes simulations have been conducted to investigate the flow field and mixing characteristics of hydrogen low-pressure direct injection for a hollow cone injector in a constant volume chamber. The 3D-CFD injector model was validated with the experimental data, and a sensitivity analysis of the CFD model parameters was performed. The study also examined the influence of fuel injection pressure and needle lift to evaluate the trade-off between them to achieve optimal mixing performance.

Key findings of the sensitivity and error analysis of the CFD model parameters:

- The combination of a medium mesh configuration with a base mesh of 1 mm, a second-order central difference spatial discretisation scheme, a first-order upwind time integration scheme, and the RNG k-ε turbulence model, along with a CFL number of 1 and a turbulent Schmidt number of 0.56 has been identified as the best balance between accuracy and computing cost in predicting the flow field and mixing characteristics of low-pressure hydrogen direct injection for the hollow cone injector.
- The error analysis of the CFD parameters revealed that the configuration consisting of a medium mesh, CFL number 1, Sct of 0.56, and the RNG k-ε turbulence model demonstrated the capability of providing valid predictive accuracy with a mean absolute percentage error of around 10.9%.

Key findings of the flow field and jet mixing characteristics with respect to injection pressure and injector needle lift:

- Due to the expansion of the effective hydraulic flow area, the augmentation in mass flow rate and the rise in jet momentum, an increase in injection pressure and needle lift, under constant chamber pressure, results in a greater volume of fuel ejected from the nozzle. This also enhanced both radial and axial jet penetration, with a more significant impact observed on radial jet distribution.
- Higher injection pressure and needle lift boosted jet exit velocity and momentum flux, thereby improving vortex formation and generating small-scale turbulence. In the 35 µm and 85 µm needle lift scenarios, increasing the NPR from 10.35 to 25.5 and 50 caused the turbulent kinetic energy at each NPR to rise by over two and three times, respectively.
- The scenario characterised by an 85 µm needle lift and an injection pressure of 20.7 bar yielded superior outcomes in terms of axial jet penetration, leading an average increase of 5.5% and 9%, compared to the 35 µm and 135 µm scenarios, whereas the combination of a 135 µm needle lift and an injection pressure of 12.68 bar proved to be optimal for radial jet penetration, resulting in an average 6% and 8.5% improvement compared to the 35 µm and 85 µm scenarios
- The scenario involving a 135 µm needle lift and an injection pressure of 12.68 bar demonstrated the highest iso-surface volume, indicating optimal distribution and mixing efficiency. It suggests that utilising a reduced injection pressure while keeping a constant fuel mass, along with increased needle lift, can achieve effective fuel-air mixing within the chamber.
- At an injection pressure of 51 bar and a needle lift of 35 µm, multiple zones of higher vorticity and substantial jet momentum were observed, alongside minor jet disturbance. Consequently, this

phenomenon resulted in a significantly elevated turbulent kinetic energy, approximately double compared to other scenarios.

The scope of future work is to apply the developed and validated 3D-CFD injector model to simulate non-reacting mixing and reacting combustion characteristics in a low-pressure direct injection hydrogen combustion engine aiming for efficiency improvement and output performance.

CRediT authorship contribution statement

B. Fil: Writing – original draft, Visualization, Validation, Software, Methodology, Investigation, Formal analysis, Data curation, Conceptualization. **C.J. Ramsay:** Writing – review & editing, Methodology, Investigation, Conceptualization. **K.K.J. Ranga Dinesh:** Writing – review & editing, Supervision, Resources, Project administration, Methodology, Investigation, Conceptualization.

Declaration of competing interestinterest

The authors declare that they have no known competing financial interests or personal relationships that could have appeared to influence the work reported in this paper.

Acknowledgements

The first author would like to acknowledge the support from the Turkish Ministry of National Education by providing the fully funded PhD scholarship known as the Overseas Graduate Education Scholarship Program (YLSY) based on Law No.1416.

References

[1] International Energy Agency. Global Energy Review 2021. https://www.iea.org/reports/global-energy-review-2021. [Accessed 6 January 2026].
[2] W.R. Institute. Climate watch. https://www.climatewatchdata.org/. [Accessed 6 January 2026].
[3] Caglayan D, Heinrichs HU, Robinius M, Stolten D. Robust design of a future 100% renewable European energy supply system with hydrogen infrastructure. Preprints (Basel) 2020. https://doi.org/10.20944/preprints202010.0417.v1.
[4] Ramsay CJ, Dinesh KKJR. Numerical modelling of a heavy-duty diesel-hydrogen dual-fuel engine with late high pressure hydrogen direct injection and diesel pilot. Int J Hydrogen Energy 2024;49:674–96. https://doi.org/10.1016/J.IJHYDENE.2023.09.019.
[5] Das LM. Hydrogen-fueled internal combustion engines. Compendium of Hydrogen Energy: Hydrogen Energy Conversion 2016;3:177–217. https://doi.org/10.1016/B978-1-78242-363-8.00007-4.
[6] Hosseini SE, Wahid MA, Ganjehkaviri A. An overview of renewable hydrogen production from thermochemical process of oil palm solid waste in Malaysia. Energy Convers Manag 2015;94:415–29. https://doi.org/10.1016/J.ENCONMAN.2015.02.012.
[7] Yadav VS, Soni SL, Sharma D. Performance and emission studies of direct injection C.I. engine in duel fuel mode (hydrogen-diesel) with EGR. Int J Hydrogen Energy 2012;37:3807–17. https://doi.org/10.1016/j.ijhydene.2011.04.163.
[8] Akal D, Öztuna S, Büyükakın MK. A review of hydrogen usage in internal combustion engines (gasoline-Lpg-diesel) from combustion performance aspect. Int J Hydrogen Energy 2020;45:35257–68. https://doi.org/10.1016/J.IJHYDENE.2020.02.001.
[9] Balat M. Potential importance of hydrogen as a future solution to environmental and transportation problems. Int J Hydrogen Energy 2008;33:4013–29. https://doi.org/10.1016/J.IJHYDENE.2008.05.047.
[10] Luo Q he, Hu J Bin, Sun B gang, Liu F shui, Wang X, Li C, et al. Effect of equivalence ratios on the power, combustion stability and NOx controlling strategy for the turbocharged hydrogen engine at low engine speeds. Int J Hydrogen Energy 2019;44:17095–102. https://doi.org/10.1016/J.IJHYDENE.2019.03.245.
[11] Duan J, Liu F, Sun B. Backfire control and power enhancement of a hydrogen internal combustion engine. Int J Hydrogen Energy 2014;39:4581–9. https://doi.org/10.1016/J.IJHYDENE.2013.12.175.
[12] Kawahara N, Azimov U. Abnormal combustion in hydrogen-fuelled IC engines. In: Tingas E-Al, editor. Hydrogen for future thermal engines. Cham: Springer International Publishing; 2023. p. 459–82. https://doi.org/10.1007/978-3-031-28412-0_12.
[13] Yip HL, Srna A, Wehrfritz A, Kook S, Hawkes ER, Chan QN. A parametric study of autoigniting hydrogen jets under compression-ignition engine conditions. Int J Hydrogen Energy 2022;47:21307–22. https://doi.org/10.1016/J.IJHYDENE.2022.04.253.
[14] Wu H, Ben Houidi M, Almatrafi F, Wu B, Du J, Magnotti G, et al. Hydrogen jet characteristics with an outwardly opening piezo injector. Phys Fluids 2025;37:036103. https://doi.org/10.1063/5.0252859.
[15] Sun Z, Hong J, Zhang T, Sun B, Yang B, Lu L, et al. Hydrogen engine operation strategies: recent progress, industrialization challenges, and perspectives. Int J Hydrogen Energy 2023;48:366–92. https://doi.org/10.1016/J.IJHYDENE.2022.09.256.
[16] Goyal H, Jones P, Bajwa A, Parsons D, Akehurst S, Davy MH, et al. Design trends and challenges in hydrogen direct injection (H2DI) internal combustion engines – a review. Int J Hydrogen Energy 2024;86:1179–94. https://doi.org/10.1016/J.IJHYDENE.2024.08.284.
[17] Wu B, Sharma P, Yu T, Palombi L, Wu H, Ben Houidi M, et al. High-speed 2-D raman and rayleigh imaging of a hydrogen jet issued from a hollow-cone piezo injector. SAE Int J Adv Curr Pract Mobil 2023;6:1883–94.
[18] Zhang CH, Kim D, Lee SW, Kook S. Effect of injection timing on gas jet developments in a hydrogen low-pressure direct-injection spark-ignition engine. Int J Hydrogen Energy 2025;179:151553. https://doi.org/10.1016/J.IJHYDENE.2025.151553.
[19] Shimmura N, Oikawa M, Hata K, Mihara Y, Takagi Y. Experimental and numerical investigation of a low-pressure direct-injection hydrogen engine focusing on high thermal efficiency with near-zero emissions. Int J Hydrogen Energy 2025;194:152418. https://doi.org/10.1016/J.IJHYDENE.2025.152418.
[20] Hu Z, Yuan S, Wei H, Huang Z, Wei H, Chan SH, et al. High-pressure injection or low-pressure injection for a direct injection hydrogen engine? Int J Hydrogen Energy 2024;59:383–9. https://doi.org/10.1016/J.IJHYDENE.2024.02.018.
[21] Xie F, Liang Z, Cui B, Guo W, Li X, Jiang B, et al. Spray-to-combustion interaction in hydrogen direct injection engines: effects of injector structure and injection pressure. Energy 2025;333:137514. https://doi.org/10.1016/J.ENERGY.2025.137514.
[22] Panthi N, Garzon Alzate AF, Sharma P, AlRamadan AS, Cenker E, Magnotti G. Direct injection hydrogen combustion under leaner conditions in an optical engine using optical/laser diagnostics. Fuel 2026;407:137432. https://doi.org/10.1016/J.FUEL.2025.137432.
[23] Hu C, Hu L, Chen H, Li L, Wu Z, Deng J. Hydrogen jet characteristics of an outward-opening injector based on schlieren imaging. SAE Technical Papers, SAE International 2025. https://doi.org/10.4271/2025-01-0228.
[24] Montanaro A, Mancaruso E, Meccariello G, Allocca L. Effects of ambient and injection conditions on a high-pressure hydrogen jet for direct injection in ICE. SAE Technical Papers, SAE International 2025. https://doi.org/10.4271/2025-01-8466.
[25] Pucillo F, Piano A, Millo F, Giordana S, Rapetto N, Vargiu L. Experimental and numerical analysis of direct injection process for hydrogen-fuelled internal combustion engines. SAE Technical Papers, SAE International 2025. https://doi.org/10.4271/2025-01-0307.
[26] Huang S, Wang Y, Qian J, Li T, Chen R, Xu S, et al. Experimental characterization of high-pressure hydrogen jet mixing and combustion. Appl Therm Eng 2025;262. https://doi.org/10.1016/j.applthermaleng.2024.125276.
[27] Wang X, Sun B, Luo Q, Ling-zhi B, Su J, Liu J, et al. Visualization research on hydrogen jet characteristics of an outward-opening injector for direct injection hydrogen engines. Fuel 2020;280:118710. https://doi.org/10.1016/j.fuel.2020.118710.
[28] Lee S, Kim G, Bae C. Behavior of hydrogen hollow-cone spray depending on the ambient pressure. Int J Hydrogen Energy 2021;46:4538–54. https://doi.org/10.1016/J.IJHYDENE.2020.11.001.
[29] Kuensch Z, Schlatter S, Keskinen K, Hulkkonen T, Larmi M, Boulouchos K. Experimental investigation on the gas jet behavior for a hollow cone piezoelectric injector. SAE technical papers 2014. 2014. https://doi.org/10.4271/2014-01-2749.
[30] Ge T, Li J, Zhu M, Zhao F, Dou Z, Wei H, et al. Experimental study on combustion characteristics in a low-pressure direct-injection hydrogen engine. Fuel 2026;415:138347. https://doi.org/10.1016/J.FUEL.2026.138347.
[31] Wang B, Lin H, Bai C, Yang C, Chen Y, Zu Z, et al. Combustion and heat transfer characteristics of a heavy-duty low-pressure-direct-injection hydrogen engine with a flat-roof-and-shallow-bowl combustion chamber. Int J Hydrogen Energy 2024;96:597–611. https://doi.org/10.1016/J.IJHYDENE.2024.11.359.
[32] Lu Y, Wang Q, Qin L, Que J, Fan L, Feng L. Comparison between homogeneous combustion and stratified combustion caused by direct injection timing adjustment in lean-burn hydrogen internal combustion engine. Int J Hydrogen Energy 2025;103:1–11. https://doi.org/10.1016/J.IJHYDENE.2024.12.469.
[33] Beyer A, Di Domenico D, Beatrice C, Kulzer AC. High-pressure direct injection as enabling technology for high-power density hydrogen SI engines: experimental analysis of the influence of jet-guided combustion regimes on efficiency and abnormal combustion. Energy Convers Manag 2025;326:119497. https://doi.org/10.1016/J.ENCONMAN.2025.119497.
[34] Coratella C, Tinchon A, Oung R, Doradoux L, Dober G, Hespel C, et al. Experimental characterization of a hydrogen hollow cone jet at under-expanded conditions via schlieren technique. Int J Hydrogen Energy 2024;72:730–43. https://doi.org/10.1016/J.IJHYDENE.2024.05.411.
[35] Fleischmann M, Mirsch N, Ghanoum M, Morcinkowski B, Adomeit P, Pischinger S. Comprehensive optical and numerical investigation of hydrogen jet formation for a commercial gasoline hollow-cone injector. https://doi.org/10.4271/2025-01-0313; 2025.
[36] Tang X, Dzieminska E, Asahara M, Hayashi AK, Tsuboi N. Numerical investigation of a high pressure hydrogen jet of 82 MPa with adaptive mesh refinement: concentration and velocity distributions. Int J Hydrogen Energy 2018;43:9094–109. https://doi.org/10.1016/j.ijhydene.2018.03.089.

[37] Lee S, Hwang J, Bae C. Understanding hydrogen jet dynamics for direct injection hydrogen engines. Int J Engine Res 2023;24:4433–44. https://doi.org/10.1177/14680874231169562.
[38] Huang Z, Yuan S, Wei H, Zhong L, Hu Z, Liu Z, et al. Effects of hydrogen injection timing and injection pressure on mixture formation and combustion characteristics of a hydrogen direct injection engine. Fuel 2024;363:130966. https://doi.org/10.1016/J.FUEL.2024.130966.
[39] Moreno Cabezas K, Zaihi A, Liu X, Aljohani B, Wu H, Ben Houidi M, et al. Numerical analysis of different hydrogen injector characteristics in a constant volume chamber. SAE Technical Papers, SAE International 2024. https://doi.org/10.4271/2024-01-2693.
[40] Moreno-Cabezas K, Houidi M Ben, Zaihi A, Roberts WL, Im HG. Analysis of nozzle geometries for hydrogen direct injection internal combustion engine. Energy Convers Manag 2025;344:120245. https://doi.org/10.1016/J.ENCONMAN.2025.120245.
[41] Houidi M Ben, Moreno-Cabezas K, Zaihi A, Aljohani B, Wu H, AlRamadan A, et al. Investigating hydrogen direct injection technology: a comparative analysis of nozzle geometries for enhanced mixing in internal combustion engines. Proc Combust Inst 2024;40:105631. https://doi.org/10.1016/J.PROCI.2024.105631.
[42] Yeganeh M, Akram MS, Cheng Q, Karimkashi S, Kaario O, Larmi M. Experimental study of hydrogen jet dynamics: investigating free momentum and impingement phenomena. Int J Hydrogen Energy 2024;68:1423–37. https://doi.org/10.1016/j.ijhydene.2024.04.296.
[43] Peters N, Warnatz J. Numerical methods in laminar flame propagation: a GAMM-workshop. Vieweg+Teubner Verlag; 1982.
[44] Bird RB, Stewart WE, Lightfoot EN. Transport phenomena. Wiley; 2006.
[45] Wilke CR. A viscosity equation for gas mixtures. J Chem Phys 1950;18:517–9. https://doi.org/10.1063/1.1747673.
[46] Monchick L, Mason EA. Transport properties of polar gases. J Chem Phys 1961;35:1676–97. https://doi.org/10.1063/1.1732130.
[47] Hirschfelder JO, Curtiss CF, Bird RB. Molecular theory of gases and liquids. 1954.
[48] Bosch n.d. https://www.bosch.co.jp/tms2015/en/products/pdf/Bosch_di_folder.pdf. [Accessed 27 May 2025].
[49] Engine combustion network. n.d. https://ecn.sandia.gov/. (accessed May 27, 2025).
[50] Tominaga Y, Stathopoulos T. Turbulent schmidt numbers for CFD analysis with various types of flowfield. Atmos Environ 2007;41:8091–9. https://doi.org/10.1016/J.ATMOSENV.2007.06.054.
[51] Feng Y, Ren X, Li X, Gu C. A variable turbulent schmidt number model in Jet-in-Crossflow simulation and its applications. Int J Heat Mass Tran 2024;234:126145. https://doi.org/10.1016/J.IJHEATMASSTRANSFER.2024.126145.
[52] Scarcelli R, Wallner T, Matthias N, Salazar V, Kaiser S. Numerical and optical evolution of gaseous jets in direct injection hydrogen engines. SAE Technical Papers 2011. https://doi.org/10.4271/2011-01-0675.
[53] Ramsay CJ, Dinesh KKJR. High pressure direct injection of gaseous fuels using a discrete phase methodology for engine simulations. Int J Hydrogen Energy 2022;47:2017–39. https://doi.org/10.1016/J.IJHYDENE.2021.10.235.